U

ULTRASONIC HYPERTHERMIA.

See HYPERTHERMIA, ULTRASONIC.

ULTRASONIC IMAGING

OLIVER KRIPFGANS
University of Michigan
Ann Arbor, Michigan

INTRODUCTION

Medical imaging has many modalities and most of them provide clinicians with unique features of a volume of interest (VOI) resulting from a chosen modality. Ultrasonic imaging is one technique for collecting anatomical and physiological information from within the human body. It can be used for diagnosis (imaging) and for image-guided therapy, where therapeutic intervention can be applied with direct image-based feedback. Other modalities include X ray (roentgen radiation), CT (computed tomography), MRI (magnetic resonance imaging), PET or PET/CT (positron emission tomography), and SPECT (single photon emission computed tomography). In contrast to most other imaging techniques, ultrasonic imaging is very attractive to professionals because it is cheap, real time (with >100 full frame images per second, >100 Hz), and it uses nonionizing radiation. Moreover, current clinical ultrasound machines can be integrated into laptop computers with very little external hardware for maximum portability and versatility. These combined features allow the use of ultrasonic imaging in a wide variety of settings, from private physician practices, to ambulances with on-site paramedics, to battle field situations, where very robust and lightweight equipment is required. Many other uses of ultrasonic imaging are found in science and industry these include, for example, ultrasonic microscopy, nondestructive testing and touch sensitive screens.

PHYSICAL PRINCIPLES

Ultrasonic imaging is based on ultrasound, which is sound produced at frequencies beyond those detectable in human hearing, that is, >20 kHz. In the same way that ultraviolet (UV) light is invisible to the human eye, ultrasound is inaudible to the human ear. Often objects that serve as carriers for ultrasound waves need to be treated as waveguides. Nonlinear effects become apparent for ultrasound propagation when leaving the range of elastic deformation during the propagation of waves through a medium. Physical material constants form ultrasound parameters, for example the speed of sound or the attenuation of sound. Very high frequency sound waves are treated by quantum acoustic laws. Historically, ultrasound was produced by oscillating platelets (1830), or pipes (1876). Magnetostriction (1847) and the piezoelectric effect followed (1880 by Curie), and are still very much relevant mechanisms for medical and industrial ultrasound. In 1918, it was found that the use of oscillating crystals could be used to stabilize frequencies. The upper frequency for sound in a given solid material is determined by the separation of neighboring atoms in the host medium. This upper frequency limit is met when neighboring atoms, assuming the linear chain model, oscillate with a 180° phase shift, the so-called optical branch of oscillations in a solid (1–15).

Sound Waves

Sound waves are mechanical waves by nature and a medium is needed to carry them. These spatial–temporal oscillations occur nonsynchronously throughout a medium and cause density fluctuations, which in turn cause temperature oscillations if the rate of such fluctuations is larger than the time constant for thermal equalization. Typical properties to describe sound waves are

Displacement $\boldsymbol{s} = \boldsymbol{s}(\mathrm{t})$ of a particle due to a traversing wave
Sound particle velocity $\frac{d}{dt}\boldsymbol{s} = \frac{d}{dt}\boldsymbol{s}(t) = v(t)$
Instantaneous mass density $\boldsymbol{\rho} = \boldsymbol{\rho}(t)$
Instantaneous pressure $\boldsymbol{p} = \boldsymbol{p}(t)$

where the later most is the deviation from the ambient static pressure. Mechanical properties, such as strain tensor σ_{ij} and stress tensor s_{ij} can be used to develop relationships between the above mentioned properties of sound waves (Fig. 1).

For mostly lossless media, such as water, one can use the laws of conservation of momentum and conservation of mass to derive the wave equation for sound waves,

$$\nabla p(r) = \frac{1}{c^2}\frac{\partial^2}{\partial t^2}p(r) \qquad \frac{B}{A} = \mathrm{const}\left[\frac{\partial c}{\partial p}\right]_T + \mathrm{const}\left[\frac{\partial c}{\partial T}\right]_p \quad (1)$$

where spatial variations in pressure ∇p are coupled to temporal variations $(\partial p)^2/(\partial t^2)$ via the speed of sound c. This simple relationship represents only a linear approximation, and is therefore valid only for waves of small displacements. The isentropic nonlinearity parameter B/A measures the amount of density change (ρ, $c = (\rho K)^{-1/2}$ (see Eq. 10) for a given pressure (p) and temperature (T) (6). Note that only second-order temporal derivatives in the pressure result in a spatial pressure change, that is, only accelerations can result in sound.

Planar and Spherical Waves. In general, mechanical waves can either travel as longitudinal waves by compressing and expanding the host medium itself or as transversal waves by exerting shear force on the host medium. Water is a very good host medium because it bears minimal

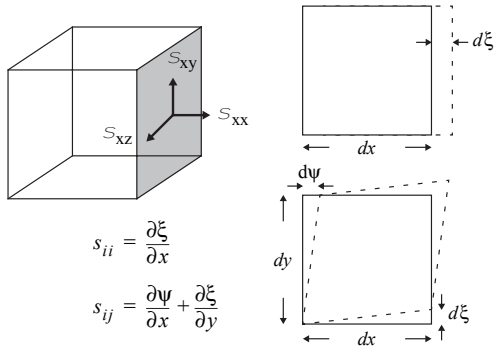

Figure 1. Ultrasonic waves travel through media by elastic deformation of matter. This deformation can be written in terms of strain σ_{ij} and stress s_{ij} tensors.

energy loss for traveling sound waves. The human body is 55–60% (8) composed of water, which ensures good acoustic accessibility. Exceptions are areas blocked by either bone or air, since bone and air provide poor ultrasound transmission characteristics. However, water mostly supports longitudinal waves. Transverse waves are attenuated at a high rate in water and can therefore be neglected. The three-dimensional (3D) wave equation in Eq. 1 reduces then to a one-dimensional (1D) equation with the general solution of an inward and outward propagating wave:

$$\left.\begin{aligned} p(x,t) &= F(x-ct) + G(x+ct) \\ p(r,t) &= \frac{1}{r}(F(r-ct) + G(r+ct)) \end{aligned}\right\} \quad \begin{matrix}\text{for Planar and} \\ \text{spherical waves}\end{matrix} \tag{2}$$

where x and r are the direction of propagation, t is time, and F and G are general, but continuously differentiable functions. The rationale for these arbitrary functions is their argument $x \pm ct$ and $r \pm ct$. This expression ensures the character of the wave as a traveling entity. Whatever the function F represents at time $t = 0$ at position $x = 0$, it will travel to position x/c after time t. In other words, by keeping the argument of the function $F = 0$, one can compute where and how fast the wave travels. Vice versa for the function G, except that it travels in the opposite direction (Fig. 2). For harmonic waves, these two functions are represented by harmonic functions, that is, sin, cos, or more general e^{ix}. Planar and spherical waves follow as:

$$\begin{aligned} p(x,t) &= pe^{ik(x \pm ct)} && \text{planar waves} \\ p(r,t) &= \frac{p}{4\pi r} e^{ik(r \pm ct)} && \text{spherical waves} \end{aligned} \tag{3}$$

Here, k is the wave number, defined as $2\pi/\lambda$, which is the conversion between spatial coordinates of wavelength to

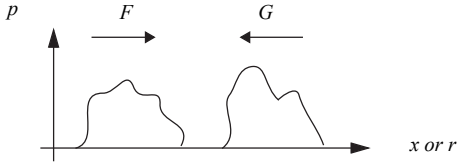

Figure 2. Illustration for the general solution of equation 1; two traveling waves F and G in opposing directions, $+r$ and $-r$, respectively.

radians in the complex exponential. Acoustic attenuation or absorption can be mathematically written as a imaginary valued wave number k_i, leading to the complex valued total wave number $k = k_r + k_i$.

Quantifying Sound

Sound intensity $I(\mathrm{W \cdot cm^{-2}})$ and acoustical power P [W]

$$\boldsymbol{I} = \overline{p\boldsymbol{v}}, \quad P = \oint_S \overline{p\boldsymbol{v}}_n dS \tag{4}$$

are measures of the strength of the acoustic waves. In both equations, the temporal average of the product of pressure and particle velocity is computed. In the equation for intensity in equation 4, the temporal average value is a vector quantity, while in the equation for power it is a scalar because the velocity is taken as the normal component to the encapsulating surface element dS. In addition to acoustic intensity and power, very often one refers to a measure for the acoustic pressure. In SI units, pressure is given by Newton per square meter $(\mathrm{N \cdot m^{-2}})$. However, sound pressures extend over a large range, and therefore a logarithmic scale, the dB scale, is commonly used to measure pressure.

$$\text{dB value} = \begin{cases} 20 \cdot \log p_{\mathrm{rms}}/p_{\mathrm{ref}} \\ 10 \cdot \log I_{\mathrm{rms}}/I_{\mathrm{ref}} \end{cases} \tag{5}$$

As can be seen from Eq. 5, a reference value must be used to compute the pressure level on a dB scale. Typically, this reference is chosen to be the peak output level of the system under test or it can be a fixed value such as when 1 mW into 50 Ω is used on some oscilloscopes. Sound pressure level (SPL) and sound intensity level (SIL) reference values in underwater ultrasonics are 1 μPa and $10^{-12}\,\mathrm{W \cdot m^{-2}}$, respectively. In contrast, SPL for air bourne sound is 20 μPa, whereas SIL remains at $10^{-12}\,\mathrm{W \cdot m^{-2}}$.

Acoustic Impedance

Impedance is a term commonly known from electromagnetism. However, it also applies to sound waves and relates sound pressure and particle velocity in a manner analogous to Ohm's law. One distinguishes at least four types of acoustic impedance: specific acoustic impedance (z) is used to compute the transmission of an acoustic wave from one medium into another; acoustic impedance (Z) is used to estimate the radiation of sound from vibrating surfaces; mechanical impedance (Z_m) is the ratio of a complex driving force and the resulting complex speed of the medium; and radiation impedance (Z_r), which is used to couple acoustic waves to a driving source or a load driven by a force.

$\boldsymbol{z} = \boldsymbol{p}/\boldsymbol{v}$	Specific acoustic impedance
$\boldsymbol{Z} = \boldsymbol{p}/\boldsymbol{U} = \boldsymbol{z}/\boldsymbol{S}$	Acoustic impedance
$\boldsymbol{Z}_m = \boldsymbol{f}/\boldsymbol{U}$	Mechanical impedance
$\boldsymbol{Z}_r = Z/S = \int d\boldsymbol{f}s/\boldsymbol{v}$	Radiation impedance

Here, $\boldsymbol{p}$ is the acoustic pressure as a function of space and time, $\boldsymbol{v}$ is particle displacement velocity as a function of

space and time, $\boldsymbol{U}$ is a volume velocity, $\boldsymbol{S}$ is the surface that emits the sound, $\boldsymbol{f}$ is a complex driving force of the sound source, such as the force of a coil that makes the membrane of a loudspeaker move, and subsequently $\boldsymbol{u}$ is the complex speed at which the forced medium is moving.

Moreover, a quantity called characteristic impedance is analogous to the wave impedance $\sqrt{\mu/\varepsilon}$ of a dielectric medium. Its analytical form depends on the type of wave. Equation 7 shows the closed form expression for planar and spherical waves. It should be noted that the characteristic impedance for spherical waves can be complex valued and therefore pressure (p) and velocity (v) are not required to be in phase.

characteristic impedence:

$$\begin{aligned} z &= \frac{p}{v} = \rho_0 \cdot c && \text{For planar waves} \\ z &= \frac{p}{v} = \rho_0 c \cdot \frac{kr}{(1+(kr)^2)^{1/2}} e^{j\theta} && \text{For spherical waves} \end{aligned} \tag{7}$$

For these two special cases one can see that planar waves have pressure (p) and particle velocity (v) in phase. The ratio of pressure to velocity is a real number and is constant ($\rho_0\ c$). Spherical waves, however, behave differently. Pressure and particle velocity are out of phase when measured close to the sound source. The ratio of pressure to velocity is a complex value (due to the $e^{j\theta}$ term and $\cot\theta = kr$) and it changes with distance (r). For large r, the spherical wave solution approaches the planar wave solution, that is, when $kr \gg 1$.

The parameter Z, the acoustic impedance, is often referred to as a frequency independent constant. The importance of this property lies in the nature of ultrasound. When imaging the human body, the sound waves travel through many layers of varying impedances, such as skin, fat, connective tissues, and organs. The crossing of each tissue boundary changes the sound waves in several ways. Typically, sound both transmits and reflects from tissue layers. While sound is mostly transmitted, small reflections are recorded and displayed as gray levels in a so-called B-mode image, where larger amplitudes of reflected waves is displayed as brighter pixels. More complicated scenarios include mode conversion between longitudinal and transverse waves. Reflection and transmission coefficients for pressure are directly related to the *change* in acoustic impedance as given in the following equation:

$$R = \frac{Z_2 - Z_1}{Z_2 + Z_1} \quad T = \frac{2Z_2}{Z_2 + Z_1} \quad 1 + R = T \tag{8}$$

Here Z_1 and Z_2 are the impedances of the proximal and distal side of the interfacial surface. Therefore, no reflection will be seen from sound entering a layer of equal impedance, but varying density and speed of sound compared to the current medium. Reflection and transmission coefficients for intensities are derived by squaring R and T in Eq. 8 (Fig. 3).

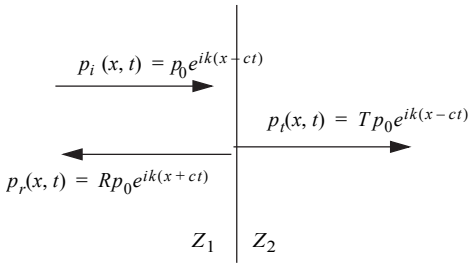

Figure 3. Acoustic propagation is altered when sound waves encounter an impedance change (Z_1 to Z_2), that is, a change in the product of local speed of sound and mass density.

Attenuation

Acoustic attenuation manifests itself in many ways. Sound can be attenuated by mechanisms of reflection, absorption, or scattering. Reflection is caused by impedance changes, whereas absorption and scattering occur due to the internal structure of the medium. Viscous forces cause sound absorption following Lambert–Beer–Bouguer's law

$$\begin{aligned} dI &= -\beta I dx \\ I(x,\beta) &= I_o e^{-\beta x} \\ p(x,t) &= p(x=0,t) \cdot e^{ikx \pm ct + ik_i x} \end{aligned} \tag{9}$$

where k_i is imaginary, and therefore $p(x,\ t)$ decays exponentially for $x > 0$. In general, acoustic waves in medical imaging are attenuated by traveling through layers of different tissues due to reflection and also due to attenuation inside tissue. Typical acoustic attenuation in biological tissues is of the order of 0.1–1.0 dB $\text{MHz}^{-1} \cdot \text{cm}^{-1}$, that is, a acoustic wave of 1 MHz center frequency, which travels 0.5 cm deep into tissue (1 cm round trip), is diminished by 0.1–1.0 dB, or its amplitude is reduced by ~1–11%. However, a 2.25 MHz wave penetrating the abdomen to a depth of 15 cm at 0.7 dB $\text{MHz}^{-1} \cdot \text{cm}^{-1}$, will be amplitude attenuated by 47.25 dB or 99.6%. Good ultrasound systems have signal to noise and amplification capabilities up to 120 dB, and therefore allow penetration to a reasonable depth at megahertz frequencies. Typical frequency selections are 7.5–15 MHz for 1–3 cm depths and 2.25–3.5 MHz for 12–15 cm depths.

Pulse–Echo

Most medical imaging via ultrasound uses a pulse–echo method to obtain images. That is, sound waves are transmitted into the body and echoes from within the body are registered, and their origin is computed using complex algorithms. Pulse–echo is somewhat unique to ultrasonic imaging. Other modalities use transmission (X ray and CT) or register preexisting radiation from within the body (PET, SPECT).

Multiple transmissions at the same physical location can reveal the motion of targets. A fundamental assumption is the speed of sound in the investigated volume. Typically, water is assumed to be 1485 $\text{m} \cdot \text{s}^{-1}$, and human tissue varies between 1450 and 4080 $\text{m} \cdot \text{s}^{-1}$ (see Table 1), with an average soft tissue value of 1540 $\text{m} \cdot \text{s}^{-1}$ (6). In general, the speed of sound is inversely related to the compressibility K ($\text{m}^2 \cdot \text{N}^{-1}$) and mass density ρ ($\text{kg} \cdot \text{m}^3$)

Table 1. Speed of Sound in Various Human Tissues[a]

Tissue	Mean Velocity, $m \cdot s^{-1}$	Tissue	Mean Velocity, $m \cdot s^{-1}$
Air	330	Brain	1541
Fat	1450	Blood	1570
Human tissue (mean)	1540	Skull bone	4080
		Water	1485

[a]See Ref. 6.

of the host medium:

$$c = \frac{1}{\sqrt{\rho K}} \tag{10}$$

Figure 4 shows the radio-frequency (rf) data for three firings at a set of moving targets. In this depiction, one can assume that the firings shown in a–c occur at a 1 ms interval. As time progresses, the scatterers move farther away from the transducer. At (a) the particles are $1/2 \cdot 26\,\mu s \cdot 1485\,m \cdot s^{-1}$, that is, 19.3 mm, away from the transducer; in (b) the particles shifted to $1/2 \cdot 32.5\,\mu s \cdot 1485\,m \cdot s^{-1}$, that is, 24.1 mm, away from the transducer. This shift of 6.5 μs or 4.8 mm is related to the interfiring time referred to by either pulse repetition interval or frequency (PRI or PRF). A PRI of 1 ms leads to the conclusion that the set of particles is moving at a speed of $4.8\,m \cdot s^{-1}$.

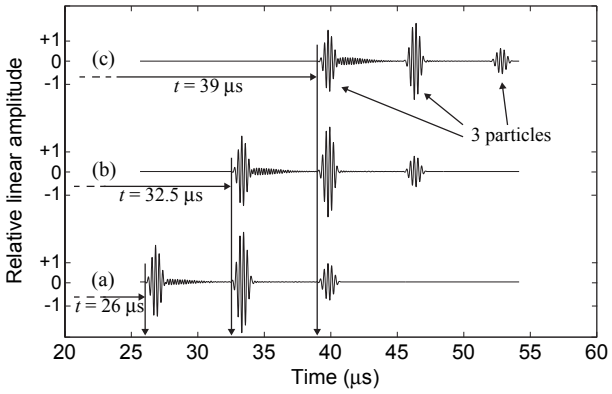

Figure 4. A set of three particles in water moves away from the ultrasound transducer during a set of three transmissions and receptions. (a) At time $t = 0$ ms the first backscatter signal of the set is received after 26 μs. (b) For the second acquisition the first backscatter is received at 32.5 and 39 μs at (c). Signal travel time is directly related to travel distance by means of the speed of sound.

ULTRASOUND GENERATION

Physics

Sound is produced by anything that moves in an accelerated fashion. Nowadays, most practical materials are piezoelectric, such as quartz (SiO_2), polyvinylidene fluoride (PVDF), and lead zirconate titanate (PZT). Piezoelectricity is an effect that is associated with the crystalline structure of the materials. A piezoelectric crystal yields a voltage across its surface when under strain, and the reverse effect facilitates mechanical oscillations of the crystal in response to an alternating current (ac) electric field applied across its surface.

Transducer Construction

Ultrasound transducers are made from piezoelectric materials, as described above. Typically, a layer of material is used to create a surface area for creation and transmission or reception of ultrasonic waves. The thickness of this layer is a function of the material properties and the desired acoustic frequency. As seen in Fig. 3, acoustic waves are reflected by impedance changes. An oscillating layer of piezoelectric material produces mechanical waves that propagate in the oscillation direction. These waves can be either compressional or shear waves. Here, the focus will be on compressional waves. Constructive interference of waves launched or reflected from the front surface and from the back surface of the crystal yield maximum pressure generation. High frequency transducers are made from very thin crystals due to their short wavelength and low frequency transducers are made from larger thickness crystals. For example, a 4 MHz transducer can be made from a 0.55 mm thick crystal. Table 2 lists the speed of sound in PZT_{5A} as $4400\,m \cdot s^{-1}$. The wavelength in PZT_{5A} at 4 MHz is 1.1 mm. Transducer crystals are typically machined to a thickness of $\lambda/2$, that is, 0.55 mm for 4 MHz. The rationale for this thickness is in the constructive interference of acoustic waves inside of the crystal. Figure 5 shows the bottom of the crystal moving up and down. Mechanical waves will launch from this surface and travel to either side of it. Assume that the

Table 2. Piezoelectric Properties of Typical Materials Used for Fabrication of Ultrasound Transducers

Property	Units	PVDF	PZT_{5A}	Quartz (x-cut)
Density	$g \cdot m^{-3}$	1.78	7.6	2.6
Relative permitivity	$\varepsilon/\varepsilon_0$	12	1700	4.52
Elastic modulus	$10^{10} N \cdot m^{-1}$	0.3	4.9	
Piezoelectric constant	$10^{-13} C \cdot N^{-1}$	$d_{31} = 20$	$d_{31} = 180$	
		$d_{33} = 30$	$d_{33} = 360$	
Coupling constant		0.11	$k_{31} = 0.35$	
			$k_{33} = 0.69$	
Speed of sound	$m \cdot s^{-1}$		4400	5740
Characteristic impedance	MRayl			15.2

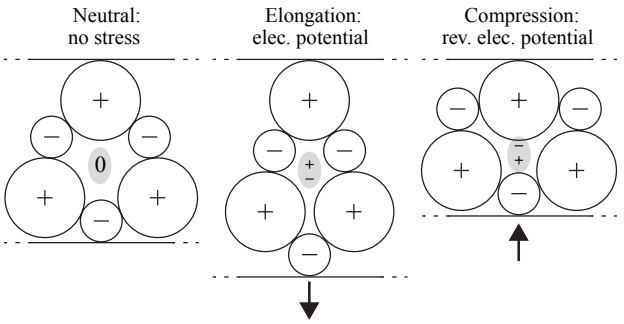

Figure 5. A piezoelectric crystal exhibits an electric charge on its surface when under mechanical stress (shown as the elementary cell response). The reverse effect is used to produce ultrasound; applying an alternating electrical potential across a piezoelectric crystal causes the crystal to vibrate along a given direction.

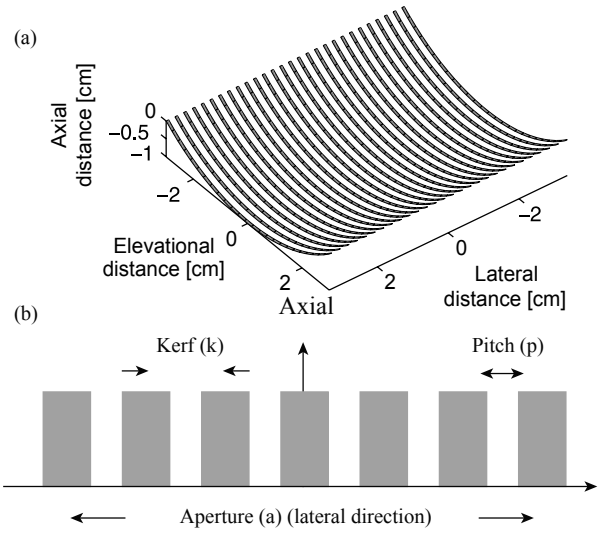

Figure 6. (a) Schematic of the piezoelectric elements of an array ultrasound transducer. Elevational curvature as well as spacing (white area, called kerf) between shaded elements is exaggerated. (b) Definition of geometric parameters: kerf, pitch, and aperture.

bottom side of the surface is facing air and that there is no sound transmitted into it. The sound wave traveling toward the top surface will be transmitted beyond that surface into the desired medium (e.g., tissue).

Reflected waves will travel downward and interfere with upward traveling waves. Moreover, reflected waves experience a phase shift of 180°. This is the reason that $\lambda/2$ is the required thickness and not λ.

Array Design. Modern clinical ultrasound imaging arrays are composed of hundreds of individual piezoelectric elements. Mostly these elements are arranged in a linear, 1D fashion, hence their name: linear arrays. The 3D in front of an imaging array are denoted axial, lateral, and elevational. Axial and lateral axes lie in the imaging plane, with the axial distance extending away from the transducer. The lateral axis is parallel to the transducer surface, inside the imaging plane, whereas the elevational axis extends perpendicular to the imaging plane. By convention, the origin is located at the transducer surface in the middle of the active aperture (see the section Acoustic Imaging). Each element may be rectangular with a fixed curvature for focusing in the elevational direction. Curvature as well as the elevational size of each array element determine the thickness of an image plane, which can be 1 mm. Typical element widths range from $\lambda_m/2$ to $3/2\ \lambda_m$. The wavelength λ_m is the wavelength within the medium where the wave is launched. Arrays with element sizes of $\lambda/2$ or smaller are referred to as fully sampled. Element sizes are typically 0.5–1 cm in the elevational direction and hundreds of micrometers in the lateral direction. The size of the space between individual elements is called the kerf (Fig. 6) and it is meant to diminish acoustic crosstalk between adjacent elements. A major design criterion for arrays is the distance between the centers of elements, called pitch. This distance determines the location and amplitude of acoustic grating lobes. Variations in the pitch, either due to changes in kerf or element width cause the grating lobes to shift. Moreover, the total extent of the aperture is directly related to the full width at half the maximum (fwhm) amplitude of the main lobe and the location of the side lobes. Equation 11 gives the fwhm of the main lobe and the angular position of the side lobes as well as grating lobes. Side lobes result from a transmit and receive aperture being small relative to the wavelength of the acoustic wave (λ/a), whereas grating lobes result from a steered and undersampled aperture, that is, an aperture with too few elements per wavelength.

$$\begin{aligned} &\text{fwhm main lobe} && \Lambda = \frac{aw}{p} \\ &\text{side lobes} && \theta_s = \arcsin\frac{\lambda n}{a} \quad n \in N_0 \\ &\text{grating lobes} && \theta_g = \arcsin\frac{\lambda n}{p} \end{aligned} \tag{11}$$

The consequence of improper selection of pitch and kerf for a given frequency is illustrated in Fig. 7a. At an imaging depth of 10 cm one can see a main lobe of almost 3 mm fwhm and strong side lobes and grating lobes. In this case the ratio of λ to element pitch is 0.4. For a ratio of λ to element pitch of 1.6, the width of the main lobe is 1.2 mm and the side lobes are mostly suppressed (Fig. 7b). Moreover, the grating lobes have disappeared when the ratio of λ to element pitch is increased.

High spatial resolution imaging is achieved by a proper selection of these geometry factors. Of additional importance to the acoustic field pattern are acoustic output, field of view, and practicality. The smaller the actual radiating area, the lower the acoustic pressure in the generated field. Moreover, a large pitch and/or element width will, for a given number of elements, cause the active aperture to increase in size, which limits the possible shift of the active aperture across the physical aperture of the array (see the section Acoustic Imaging). A

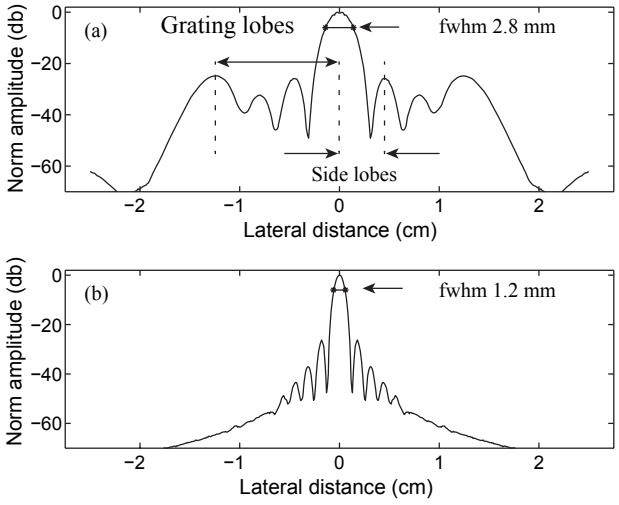

Figure 7. (a) Four elements (200 μm kerf, 1000 μm pitch) using 4 mm aperture, yield a main sound lobe width of 2.8 mm fwhm. (b) Forty elements (50 μm kerf, 250 μm pitch) using 1 cm aperture, cause the main lobe to narrow to 1.2 mm fwhm and the sidelobes and grating lobes to diminish. Half maximum corresponds to −6 dB.

large number of elements is beneficial for focusing and field geometries, but it is physically difficult to electrically wire a substantially larger number of elements. Furthermore, it directly increases costs, since each element requires cabling and multiplexing electronics. Channels with transmit and receive electronics are in general multiplexed to the physical elements. The complications involved with cabling hundreds or thousands of elements as well as the challenge of real-time data acquisition of a large number of channels are directly related to the still limited usage of two-dimensional (2D) imaging arrays. A good introduction and very detailed overview can be found in Shung and Zipparo (16), as well as Angelsen et al. (1,17).

Acoustic Fields. Acoustic fields of transducers can be analytically derived from basic principles. Logically, this derivation originates at the sound source, a moving object or surface. Its motion and surface shape/orientation define the so-called source strength Q (Eq. 12). Using this source strength one can compute the actual pressure field at a distance r from the source. In order to do so, it is necessary to derive the fact that for all simple geometries, the ratio of source pressure P_1 to its source strength Q_1 and the ratio of a second source pressure P_2 to its source strength Q_2 are equal at the same distance (assuming the same frequency). However, the derivation of this equality is beyond the scope of this text. The pressure of a circular piston can now be written as a function of its source strength, as well as the pressure and source strength of a known source, typically a small sphere. Equation 13 gives the analytical expression for the pressure field of the piston transducer, where r is the distance of the observation point from the center of the aperture, θ is the angle between the axis extending perpendicularly from the center of the transducer and the line from the center to the observation point, t is time, ρ is the mass density of the surrounding water, c is the speed of sound in water, U_0 is the sound particle velocity on the aperture, and ω and k are angular frequency and wave number, respectively. The integral is simplified for circular geometry and taken over the entire surface of the transducer's aperture. In *real* world simulations, one could take into account that the circumference of the aperture might be clamped or for other reasons not be able to oscillate with the same amplitude as the center of the aperture. To do so, one would keep U_0 inside the integral as a function of radius or even radius and in-plane angle of the aperture.

$$Q = \int_S (\boldsymbol{u} \cdot \boldsymbol{n}) dS \tag{12}$$

$$\frac{P_1}{Q_1} = \frac{P_2}{Q_2} \Rightarrow P_p = \frac{P_s}{Q_s} Q_p$$
$$P_p = \frac{\rho c}{-i2\lambda r} \int_S (\boldsymbol{u} \cdot \boldsymbol{n}) dS \tag{13}$$
$$P_p(r, \theta, t) = \frac{i\rho c U_0}{r} e^{i\omega t} \int_S \frac{e^{-ik\sqrt{r^2+s^2}}}{\sqrt{r^2+s^2}} 2\pi s ds$$

After deriving the general pressure field, one can compute special cases that are of particular interest, such as the central axis, as well as the far-field angular distribution of the radiation pattern. Further simplification of Eq. 13 yields approximate expressions for both cases and plots are shown in Fig. 8.

$$p(r, 0, t) = \rho c U_0 \left(e^{-ikx} - e^{-ik\sqrt{x^2+a^2}} \right) e^{i\omega t} \qquad \text{(central axis)}$$
$$p(r \gg a, \theta, t)$$
$$= \frac{i\rho_0 c U_0}{2r} a(ka) e^{i(\omega t - kr)} \frac{2J_1(ka \sin\theta)}{ka \sin\theta} \qquad \text{(far field)} \tag{14}$$

From the axial dependence one can see strong interference for locations close to the transducer surface. This region is called near the field or Fresnel region and it extends approximately $r = 4$ aperture diameters a away from the transducer. Beyond that point, the pressure falls off following a $1/r$ dependence, and this region is called the far field or Fraunhofer region. As a rule of thumb, the far field starts at $a^2(2\,\lambda)$. Imaging is impractical or impossible in the near field. However, one should keep in mind that this result is true only for a *single* element transducer, and subdividing the aperture into an array of small elements shifts the near-field–far-field transition toward zero based on the actual dimension of the array. Moreover, this transition point is also a function of the emitted frequency as represented by angular frequency and wave number in Eq. 13 and 14. For illustration purposes, a ka value of 8π was chosen for Fig. 8a. When plotting the angular field pattern in Fig. 8b. However, $ka = 4\pi$ was chosen to reduce the number of sidelobes and make the plot more readable. Similarly to Fig. 7, a strong main lobe and additional side lobes are evident in Fig. 8b, that interfere with the main lobe in the sense that appreciable sound will be detectable in nearly all directions. In fact, for this particular example echo amplitudes

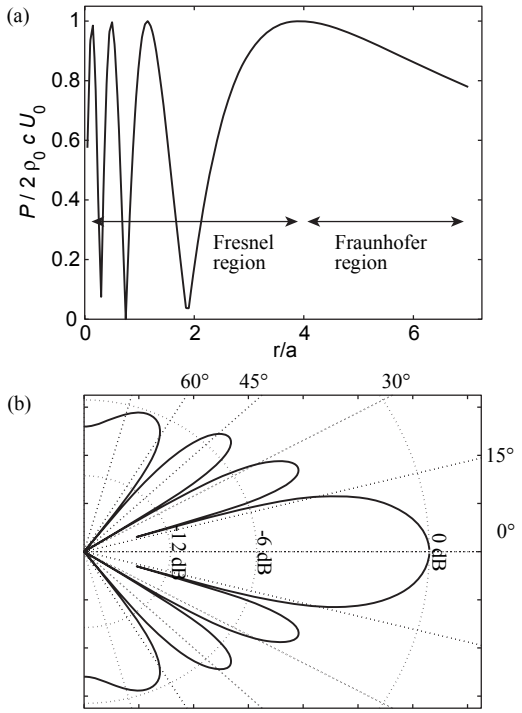

Figure 8. Acoustic field of a circular single element ultrasound source (transducer). (a) The axial transducer response can be divided into near field and far field, with an asymptotic $1/r$ dependence for large r. Phase interference is dominating in the near field. (b) Angular radiation patterns are described by the Fourier transform of the aperture function. A circular piston transducer yields a function that is defined as a Bessel function of the first type divided by its argument $[J_1(x)/x]$.

60–70° off the center axis will be only 50% lower than the main lobe. Note that this example is for educational purposes and is not at all a suitable design for imaging. Aperture sizes and frequencies as shown in Fig. 7, where a narrow and dominant main lobe can yield lateral and elevational spatial selectivity and time range gating, can yield depth information. In general, radiation patterns can be derived as Fourier transforms of the emitting aperture. Circular apertures are described by Bessel functions of the first type divided by their argument, that is, $J_1(x)/x$. For rectangular apertures the sine function $[sin(x)/x]$ directly describes the field.

ACOUSTIC IMAGING

Ultrasonic imaging yields 2D images. Pixel columns represent the lateral extent and rows of pixels display reflections of the transmitted acoustic waves from progressively deeper tissues within the body.

The most rudimentary way of obtaining lateral image data is done by using a single element transducer and wobbling it back and forth over a chosen sector. The most elegant way is to use an electronically controlled array of very small transducers and scanning and or steering an imaging beam across the region of interest. The former method is rarely used anymore. The latter method is the modern standard for ultrasonic imaging of single image planes and a few clinical scanners are even already available for 3D image acquisition of steered elevational image planes.

Depth information is encoded in the time that an acoustic wave takes to travel to a tissue site and back to the transducer. Transmitted sound can be received after a theoretically predictable wait time (see top section of Fig. 9). Such prediction requires the knowledge of the speed of sound along the traveled path. Unfortunately, an assumption of $1540\,\mathrm{m}\cdot\mathrm{s}^{-1}$ for soft tissue is not always precise. Various tissues in the human body differ from each other in terms of their specific speed of sound. When performing abdominal scans, aberration distortions can become significant due to the change in the speed of sound between connective tissues, fat layers, muscles, and abdominal organs. Other anatomical sites that provide difficulties for ultrasonic imaging include the human brain

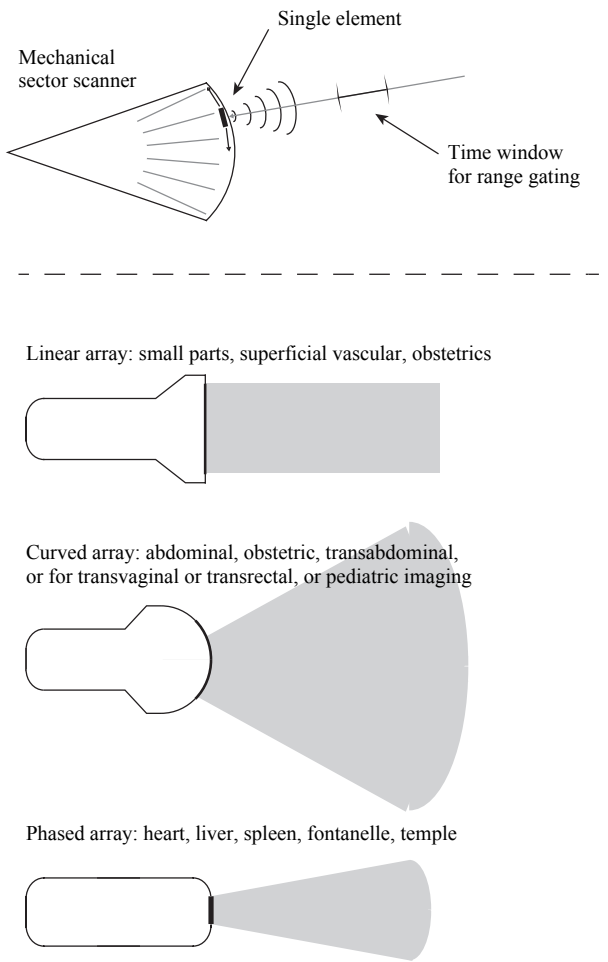

Figure 9. Transducer geometries include (curved) linear arrays and phased arrays. Linear arrays transmit and receive acoustic beams perpendicular to their surface area, whereas phased arrays steer the acoustic beam by a phasing scheme (Fig. 10).

and the heart. Fortunately, for newborns and infants ultrasound can be used to image the brain. Using a phased array (see bottom section of Fig. 9), pediatricians can image the brain directly through the fontanelle, which provides enough acoustical access for imaging. Premature newborns tend to have bleeding in the brain and develop larger ventricles, both of which can be imaged very easily through the fontanelle. However, when this acoustic access window closes, it is very difficult if not impossible to use ultrasound to image the brain. In adults, the temple fissure can be used to image (using a phased array Doppler system at 2.25 MHz) the germinal matrix near the foramen of Monroe. However, transcranial Doppler requires some guesswork on the orientation of vessels. Because of the limited access via the temple fissure, only small aperture and low frequency arrays with sub-optimal imaging capabilities can be employed.

The simplest imaging device is a linear array (range of transducer frequencies: 3–12 MHz). As its name suggests, this type of transducer has a linear arrangement of individual transducer elements. Images from a linear array are generally rectangular, and the image width corresponds to the width of the array. A set of adjacent elements (a subaperture) is used to fire a single image line or a portion thereof. Figure 10 shows how a subaperture can be used to steer and focus a beam. On the left side of each drawing, single sinusoids symbolize the electrical signals being used to excite the individual transducer elements (thick-lined vertical bars) of the array. After excitation an elementary spherically spreading wave launches from each element. Appropriate delay times applied to each electrical signal allow the ultrasound scanner to steer and focus the emitted wave front.

Additional wave conditioning includes amplitude shading of the subaperture. Typically, Gaussian-type functions or approximations thereof are used to weaken the transmit power for the outer most elements of a subaperture. The process is called apodization and yields lower side lobes since the side lobes are related to the Fourier transform of the aperture function. A gaussian apodization will result in a gaussian envelope for the side lobes, whereas no apodization (i.e., a constant amplitude excitation) would yield a sinc function $(\sin(x)/x)$ side lobe envelope.

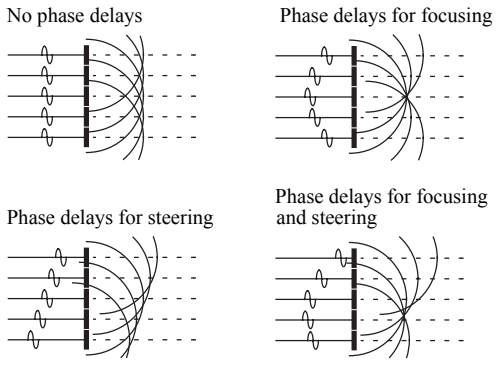

Figure 10. Delaying or advancing the phase of waves emitted from neighboring elements relative to the center element can achieve focusing and steering of the acoustic wave front.

To render an image, a subaperture is formed and linearly moved through the whole physical aperture. A major drawback of this imaging scheme is the dead time of the scanner, which occurs while waiting to receive the backscatter from the maximum depth. Fifteen centimeters of penetration require a wait time of at least (two fold for the round trip time):

$$t = \left[\frac{0.15\,\mathrm{m}}{1540\,\mathrm{m}\cdot\mathrm{s}^{-1}}\right] \times 2 = 200\,\mu\mathrm{s}$$

In addition to this delay, some additional wait time may be required to suppress echoes from even larger depths. Image lines might be separated by 250 μm. For a physical aperture of 5 cm, for example, one has to transmit and receive 201 scan lines, which is equal to a time of 200 μs * 201 lines, that is, 40.2 ms per one full frame or a frame rate of 25 Hz. This frame rate seems reasonable, but one has to keep in mind that no extra wait time was added nor any other imaging overhead such as occurs during blood flow imaging using Doppler.

Nonetheless, if one takes into account the finite lateral width of a transmitted wave, one can subdivide the total image width into independent image segments in which beams can be fired simultaneously, or at least with minimal delay (see Fig. 11). Therefore an aperture of 5 cm could eventually be imaged with five simultaneous beams or a five+fold higher frame rate. Such high frame rates allow real-time ultrasonic imaging of the body and additional overhead, such as is mentioned above for Doppler or multizone focusing. This type of focusing is used when a large depth image would cause the acoustic beam to diverge too much before and after the focal point. By firing the same image line two, three, or four times, the same number of foci can be formed for tighter acoustic beams at larger depths or for shallow regions. This scheme will work to the limit that the beams are not overlapping, that is, there is no signal coming from adjacent image lines.

Other imaging modalities, such as X ray, do not suffer from slow acquisition time due to low wave speeds. Another method to overcome the speed of sound limitation is the use

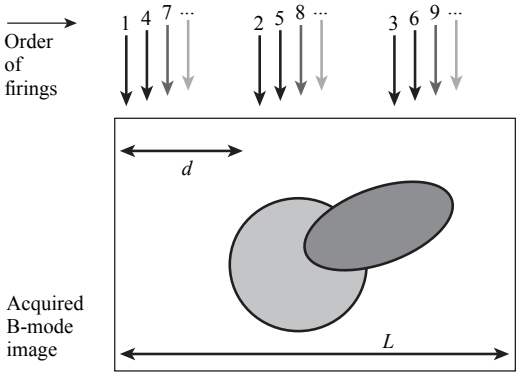

Figure 11. Interleaving scheme for image data acquisition. By minimizing the segment separation d, a maximum of L/d semisimultaneous transmit and receive zones can be achieved. The beam shape determines the smallest value of d, such that no overlap between adjacent firings will occur.

of *synthetic aperture* imaging. This method is already used in astronomy. Instead of 201 firings for 201 image lines, only one transmit is fired, and only one receive is recorded. Image reconstruction and especially spatial resolution will be computed/extracted from received data by extensive postprocessing. This scheme does not yield as much detailed backscatter data; however, it does yield very high frame rates. If only the speed of sound is limiting the data acquisition, then for the above example, the frame rate will increase by a factor of 201. Only the vast processing power of current computers makes synthetic aperture imaging possible. Typical applications for this type of image formation include full screen flow imaging, 3D, or 4D imaging (see respective subsections).

Other types of arrays include curved arrays and phased arrays which are popular for scans that require a larger image width then can be achieved by simply extending the physical aperture. Curved arrays, as seen in Fig. 9, form sector images. Because of the shape of the aperture, a relatively wide image can be achieved using a smaller footprint aperture. Scan lines are no longer parallel to each other but form a fan beam arrangement with field of view angles of up to 85° (150° for some endocavitary arrays). Typical bandwidths range from 2–8 MHz, which is a lower range than for linear arrays since this type of probe is intended for large penetration depths where frequency dependent attenuation prohibits very high frequencies. The use of nonionizing radiation to achieve real-time imaging with large fields of view makes theses probes ideal for abdominal interoperative guidance of, for example, biopsy needles or radiofrequency (RF) ablation tumor treatments. These features are also ideally suited for obstetrics (see Fig. 12).

Phased arrays are also designed to form sector images. Contrary to curved arrays, where the natural shape of the physical aperture provides the basis for the sector shape, phased arrays steer the beam to form the image. As illustrated in Fig. 10, specific timing delays for the subaperture can not only focus to a specified depth, but also steer the beam in the lateral direction. Large fields of view can be achieved this way, but the development of increased side and grating lobes are a trade-off. Anatomical locations with small diameter access to larger distal regions can be imaged with this type of ultrasound array. For example, temple access can be used to image the frontal brain, and extension of the carotid artery above the jaw line is possible. Cardiac imaging typically relies on phased arrays due to acoustic shadowing from the rib cage, where one needs to image between narrowly spaced ribs in order to interrogate the much larger sized heart chambers.

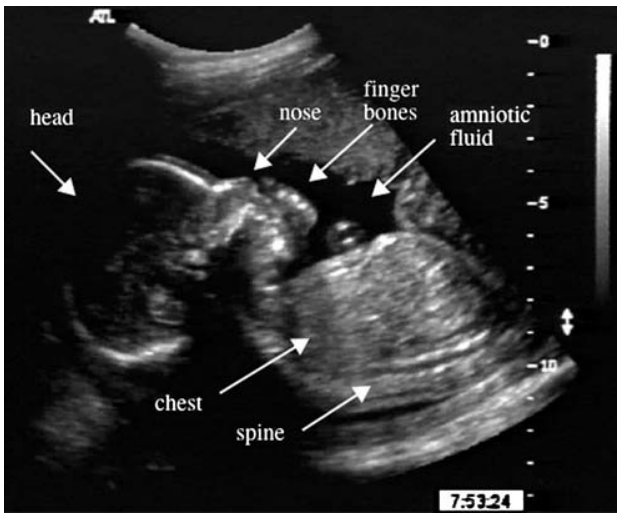

Figure 12. B-mode image of a fetus at the end of the second trimester (cross-sectional sagittal view). Low backscatter amniotic fluid is surrounding her head and upper body. The video reveals that the embryo is sucking her thumb. A curved array was used in this obstetrics exam.

B-Mode

B-mode is one of the most commonly used operation modes of a clinical ultrasound scanner. As explained earlier, ultrasound is a reflection or scattering based imaging modality, and the sophisticated generation of a sound wave allows the focusing of the sound to a specific location. Each transmission yields one scan line around the targeted focal point. If only one focal point is selected, one scan line extends over the total depth range, which is user defined in the current imaging settings. In order to record a full image frame using a linear array, the imaging software of the scanner electronically moves the active aperture of the array across the physical aperture to transmit and receive at a given line density. Typically, hundreds of scan lines are generated this way and displayed on a monitor. Figure 12 shows the cross-sectional sagittal (front to back, vertical slice) image of a fetus *in utero*. She is sucking on her thumb, as real-time video reveals. On the left of Fig. 12 one can see the head and the strong reflection of the skull bone. The very left side of the image is black, an artifact that could be due to maternal bowel gases that scatter the sound away from the transducer. The remainder of the skull is clearly visible from the forehead to the chin and from the back of the head to the neck area. Bones reflect sound waves well and result in a bright signal in the image. The black surroundings of the fetus are regions of amniotic fluid, which does not scatter sound due to the homogeneous nature of the fluid.

In front of the mouth, one can see the hand of the fetus. Once again the bones of the hand, namely, the knuckles, are pronounced since they scatter more ultrasound than the soft tissue of the hand. In the same fashion one can see the reflections of the spine.

M-Mode

M-mode (also called motion-mode imaging) does not yield full frame images per se, but rather one selected image line is rendered as a function of time. This is used for displaying motion of, for example, the periodic movement of heart valves. Any abnormalities or temporal variations can be directly seen as an image on the screen. The B-mode cross-section of a carotid artery is shown in Fig. 13a. Proximal and distal vessel wall delineates the dark vessel interior, as indicated by the arrows to the right.

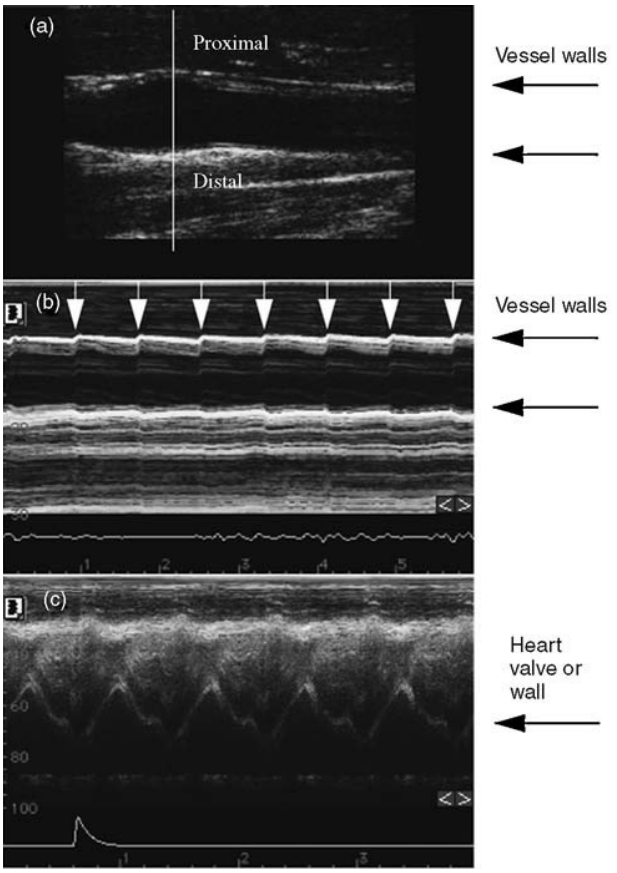

Figure 13. a. Longitudinal cross-section of carotid artery. The pixels along the vertical white line in (a) are plotted in (b) as a function of time. Black arrows indicate the proximal and distal vessel wall. Such walls are in motion as blood is pumped through the vessel in a pulsatile fashion. The repetitive pulsatile wall motion can be seen in the M-mode image in (b).

In a M-mode representation in Fig. 13b, pixels along the white vertical line in (a) are repeated parallel to each other over time. Figure 13b shows 5 s of repeated scans. For each heart beat a pulsatile wave travels through the arterial blood pool locally expanding the blood vessels. This expansion can be seen in B-mode as well as in M-mode representation. However, in B-mode it is an event in time occurring over several image frames, whereas in M-mode this event is plotted as the horizontal axis and therefore easy to detect. White arrows in Fig. 13b indicate the temporal expansion of the blood vessel. Figure 13c shows a much more pronounced motion. The transducer was pointed toward the heart and is therefore either imaging the heart wall or one of the heart valves, showing the typical cardiac pattern.

Doppler Imaging

Acoustic transmission of multiple beams along the same line can reveal temporal changes in the human body. As seen in Fig. 4, pulse echo firings in a rapid fashion can track flow, as well as flow changes in time. A more formal derivation of the mathematical framework shall follow here.

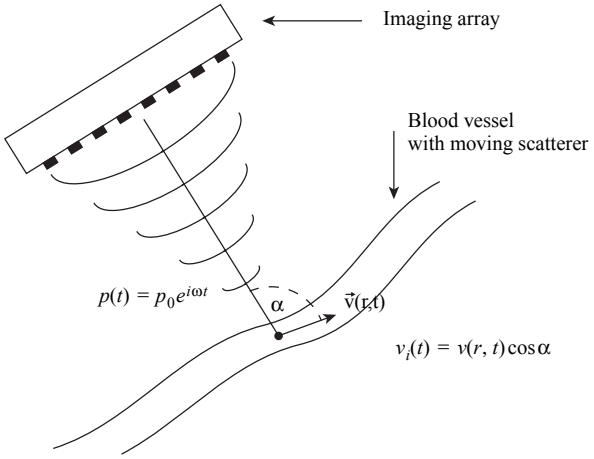

Figure 14. Illustration of Doppler imaging of a blood vessel.

Assume a vessel that is imaged at some angle a, which has acoustic scatterers such as red blood cells flowing at speed $v(r, t)$, as is depicted in Fig. 14. A recorded acoustic echo has an amplitude, frequency, and phase $(a \cdot e^{i(\omega t+\phi)})$. The measured phase is the sum of temporal and spatial phase components. The first term $\omega\Delta t$ in Eq. 15 changes in time with ω and the second term changes in time with the velocity $v(t)$ of flowing red blood cells. Flow speed $v(t)$ and direction α ($\cos\alpha$) determine the magnitude of the measurable phase shift. Due to the $\cos\alpha$ term, any displacement that occurs parallel to the aperture will not be detected.

$$\Delta\phi(\Delta t) = \omega\Delta t - 2\pi\frac{v(t)\cos\alpha\Delta t}{\lambda} = \omega\Delta t\left(1 + 2\frac{v(t)}{c}\right) \quad (15)$$

It is assumed that the time between firings Δt is small enough that the scatterer does not move out of the main lobe of the beam pattern (Fig. 7). Moreover, it is assumed that $v(t)$ is constant during Δt. The absolute and relative received Doppler shift frequency can be directly derived from the change in phase, as the temporal derivative of the phase angle (Eq. 16).

$$\begin{aligned} f_{\text{receive}} &= \frac{1}{2\pi}\frac{\partial}{\partial t}\Delta\phi(t) = \frac{\omega}{2\pi}\left(1 + 2\frac{v_i(t)}{c}\right) \\ &= f_{\text{transmit}}\left(1 + 2\frac{v_i(t)}{c}\right) \\ \Rightarrow \frac{f_{\text{receive}}}{f_{\text{transmit}}} &= \left(1 + 2\frac{v_i(t)}{c}\right) = \left(1 + 2\cos\alpha\frac{v(t)}{c}\right) \end{aligned} \quad (16)$$

In the following example, a simulated scatterer is imaged and its traveling speed is measured. In the computation, the scatterer is travelling away from the imaging array from an axial distance of 2.50–2.52 cm, that is, 200 μm. On that path, the scatterer is imaged 32 times, once every 0.36 ms. Its speed is $2\,\text{cm}\cdot\text{s}^{-1}$. Figure 15a displays the backscatter of a scatterer as shown in Fig. 4, except that only one scatterer is imaged. Thirty-two

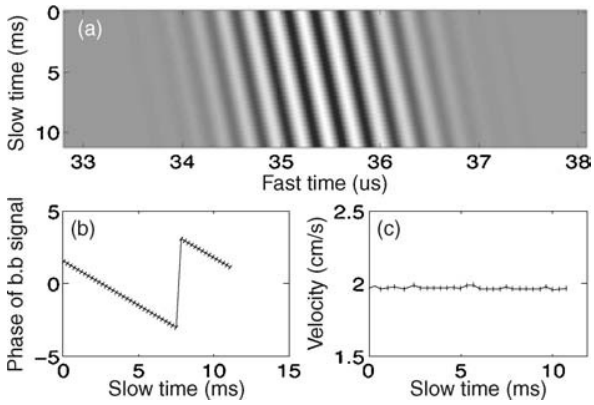

Figure 15. Doppler processing for velocity estimation. (a) Shows stacked (slow time) backscatter signals (fast time) of a moving scatterer. Complex analysis of such signals reveals the change in phase of the backscatter signal (b), and subsequently the scatterer velocity can be computed (c).

backscatter signals are stacked vertically, and the ordinate is labeled with the time at which the signal was measured ("slow" time in ms), whereas the abscissa shows the time frame of the measured radiofrequency signal ("fast" time in μs) same as in Fig. 4. This arrangement of backscatter data is very similar to that used in M-mode imaging. Signal amplitude is displayed as gray scale with gray for zero, black for negative amplitudes, and white for positive amplitudes. Two major steps are performed in order to estimate the velocity of the scatterer from the backscatter signal. At first the signal $f(t)$ is transformed into a complex valued signal $f^*(t)$ by performing a Hilbert transform (Eq. 17). Measured signals are always real valued quantities. However, for computational purposes it is desirable to have complex valued data $f^*(t)$. This step allows us to directly measure the phase of the backscatter signal and yield the velocity of the scatterer after basebanding, which is the second step.

$$\begin{aligned} f^*(t) &= \frac{1}{\pi} P \int_{-\infty}^{\infty} \frac{f(\tau)}{t-\tau} d\tau \\ &= \frac{1}{\pi} \lim_{\varepsilon \to 0^+} \left(\int_{-\infty}^{t-\varepsilon} \frac{f(\tau)}{t-\tau} d\tau + \int_{t+\varepsilon}^{\infty} \frac{f(\tau)}{t-\tau} d\tau \right) \end{aligned} \tag{17}$$

Basebanding is a mathematical procedure used to remove the carrier frequency, the main transmit frequency, from a rf-signal. For a complex valued signal, $f^*(t)$, this is done by multiplying the signal with a complex harmonic of the same, but negative frequency $(-\omega_0)$ as the carrier to obtain the complex valued envelope or amplitude modulation $a(t)$ and the phase ϕ (Eq. 18).

$$f^*(t) e^{-i(-\omega_0)t} = a(t) e^{i\phi(t)} \tag{18}$$

The phase is constant for each rf line in tissue, but varies between firings as targets, such as red blood cells, move. Figure 15b shows the phase of the basebanded signal and therefore the position of the scatterer. At ~7.5 ms, the phase wraps from $-\pi$ to $+\pi$ and continues to decrease. This phase wrap was detected and unwrapped before computing the velocity as proportional to the derivative of the phase. This phase unwrapping is not performed in clinical ultrasound scanners. Rather one will see flow of the opposite direction being displayed on the screen as the Doppler processing unit concludes that the sudden increase in phase from $-\pi$ to $+\pi$ must be due to flow in the opposite direction. This artifact is called aliasing and is typically avoided by increasing the pulse repetition frequency (PRF), that is, the rate at which Doppler firings are repeated along the same scan line in order to track backscatter from blood cells. Inverting Eq. 16 for $v(t)$ and using data processed via Eq. 17 yields the flow velocity as given in Eq. 19. A comprehensive description of medical Doppler and Doppler physics can be found in and McDicken and Evans (18).

$$v(\tau) = \frac{c}{2\omega_0} \frac{d}{d\tau} \phi(\tau) \tag{19}$$

Pulse Wave Doppler. Pulse wave Doppler (PW Doppler) is used for measuring blood flow. The user can position a Doppler scan line and Doppler window to any location within the B-mode image, as seen in Fig. 16. The two short horizontal lines at a depth of 6.9 cm in the top B-mode image in Fig. 16 represent the sample volume. This is where the Doppler data is acquired. Typically, the beamformer of the scanner is set to the same sample volume location for transmit and receive. The axial size of this window can be adjusted and is displayed on the screen (here 2 mm, see Size in the right side data column of Fig. 16). Changes in the window's size will affect the duration of the transmitted tone burst cycles. Commonly scanner software adjusts the duration of the transmit pulse to be twice as long as the chosen sample volume. Additionally, an angle (α) can be selected along which a blood vessel is oriented (here 0°, for example, along the Doppler scan line). As shown in Fig. 14 and Eq. 16, the measured flow

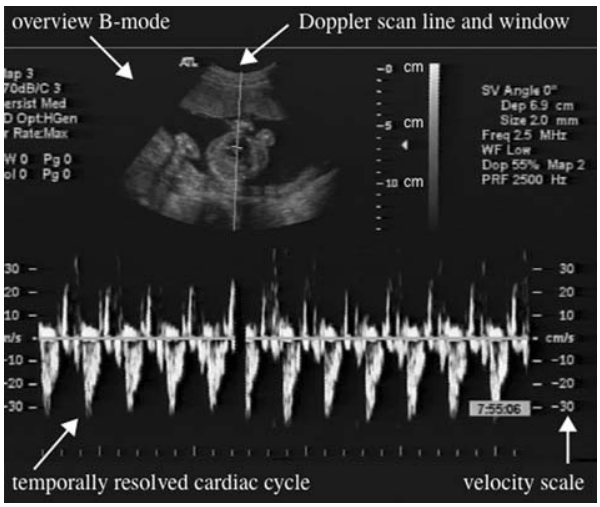

Figure 16. Pulse wave Doppler example. See text for more description.

velocity is only the projection of the actual flow vector onto the acoustic beam, which results in a cos α term. By manually choosing the correct α, the actual flow velocity can be computed and displayed from the measured flow.

The bottom part of the screen image in Fig. 16 shows the temporally resolved blood velocity, where the abscissa represents time (here, a total of 5 s), and the ordinate represents velocity (here, from -30 to $+30\,\mathrm{cm}\cdot\mathrm{s}^{-1}$).

Traditional processing computes the power at each frequency and subsequently the associated velocity, as outlined in Eq. 20.

Here the phase ϕ of the basebanded backscatter signal $a(t)e^{i\phi(t)}$ is digitized along the slow time scale (ms). Fourier analysis is used to determine the frequency or rate of change (ω_n) of the phase $\phi_n = \phi(t_n)$ More precisely, the so-called spectral power $P(\omega_n)$ at each frequency ω_n is computed by Fourier analysis. This quantity yields how much contribution to the power there is for a given rate of change or speed v_n. These two quantities $P(\omega_n)$ and v_n are plotted in the velocity graph in Fig. 16 (lower plot). The gray level for a given point in the graph is determined by $P(\omega_n)$, whereas v_n or ω_n and the time t determine the location of the pixel. The indicated cardiac cycle in Fig. 16 shows contributions from high velocities that yield high Doppler frequencies. At the end of this cycle the blood flow slows down and contributions to high frequencies diminish and formerly white pixels are now plotted in black. Other operations such as windowing of the phase signal ϕ_n are neglected here for simplicity.

$$\begin{aligned} f^*(t)e^{-i(-\omega_0)t} &= a(t)e^{i\phi(t)} \\ P(\omega_n) &= |\sum_n \phi_n T_n e^{i\omega_n n}|^2 \\ v_n(t) &= \left(\frac{\omega_n(t)}{\omega_0 T_{rep}}\right)\left(\frac{c}{2}\right)\cos\alpha \end{aligned} \tag{20}$$

Color Flow Doppler. Color flow Doppler allows the user to see a 2D map of flow in the current B-mode image. Instead of measuring flow only along a single scan line as in Pulse wave Doppler (PW Doppler), all lines inside a chosen region of interest (ROI) are fired repetitively (4–16 times) and analyzed for flow. Velocity resolution and frame rate are limited due to the large number of acoustic transmissions and the computational burden of analyzing the resulting received waveform data. In the same fashion as in B-mode, interleaved imaging can be used to counterbalance the reduction in frame rate caused by the necessary increase in (Doppler) scan lines (see Fig. 11).

In Fig. 17, one can see a regular B-mode image of a carotid artery, extending from the left to the right side of the image, parallel to the transducer face. The gray scale B-mode image is overlaid with Doppler information inside a user-defined color flow box, which is either a rectangle or a parallelogram slanted either to the left or right. For this specific example, a rhomboid with 20° rightward steering was used in order to measure the velocity of blood flow. One should remember that vessels parallel to the transducer do not yield a Doppler or phase shift and therefore can not be identified with Doppler methods. However, a 20° rightward steering provides enough angle deviation to measure flow

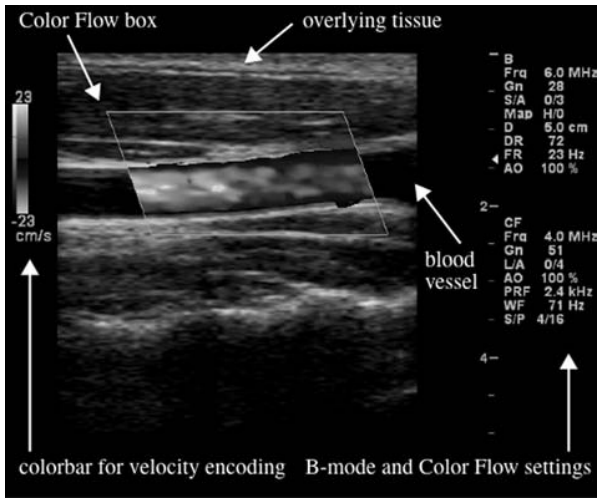

Figure 17. Color flow example showing blood flow in the carotid artery. The color data (here in gray scale) encodes magnitude and direction of flow. A color bar allows the quantitative conversion to actual speed, here a maximum of $\pm 23\,\mathrm{cm}\cdot\mathrm{s}^{-1}$.

and to display velocities everywhere in the chosen color flowbox. Ultrasonic waves are transmitted parallel to the slanted rhomboid.

Typically, blood flow is encoded from dark red to red to yellow when it is approaching the transducer, indicating low, moderate, or high velocities, respectively. Alternatively, it is colored in shades of blue to cyan when it is moving away at low to high speed. The maximum detectable velocity magnitude is directly related to the PRF used. A PRF of 2.4 kHz was chosen in the example shown, resulting in a maximum detectable velocity of $\pm 23\,\mathrm{cm}\cdot\mathrm{s}^{-1}$. Note that the PW Doppler example in Fig. 16 used a 4% greater PRF but allows a 30% greater velocity range. This is related to the greater burst length used in PW Doppler (15–20 cycles) compared to CF Doppler (2–6 cycles) and the subsequent data processing. The PW Doppler is designed for high velocity resolution and simultaneous temporal resolution, whereas CF Doppler is designed for great spatial resolution. Moreover, one should notice the very low backscatter level of blood relative to the surrounding tissue, which can be as much as 40 dB below that of soft tissue. The blood vessel in Fig. 17 appears black relative to the tissue on the proximal and distal side of it.

As mentioned above, CF Doppler demands not only more acoustic transmissions, but also more computing power to estimate the actual flow velocities from the measured acoustic backscatter. This imaging modality became practical when Kasai et al. (12) succeeded in designing a method (see Eq. 21) by which the mean Doppler frequency, that is, the mean velocity in every pixel, could be computed in real time by cross-correlations of the quadrature components, I and Q, of the analytic (complex) backscatter signal. Quadrature components I and Q are obtained by mixing the rf-signal at the hardware level with $\sin(\omega_0 t)$ and $\cos(\omega_0 t)$. This corresponds to the complex base banding given in Eq. 18, since $e^{-i\omega t} = \cos\omega t\text{-}i\,\sin\omega t$. It follows that I and Q are the real- and complex- valued parts of the

basebanded signal, $a(t)e^{i\phi(t)} = I + iQ$.

$$\phi = \frac{\Sigma_{n=1}^{N-1} Q[n]I[N+n] - I[n]Q[N+n]}{i\Sigma_{n=1}^{N-1} Q^2[n] + I^2[n]}$$
$$\bar{v} = \frac{c}{2\omega_0 T_{rep}} \arctan\phi \tag{21}$$

Power Doppler

The previous two methods of flow quantification suffer from a lack of good flow detection. In perfusion studies, it is often necessary to detect very small amounts of flow volume travelling through capillaries at velocities of the order of $1\,\mathrm{mm}\cdot\mathrm{s}^{-1}$, which is $\sim$0.1% of the speed observed in the carotid artery. In order to overcome the poor sensitivity of PW and CF Doppler, power Doppler displays the integral of the power spectrum $P(w)$, shown in Eq. 20. Typically, the integration value is also averaged over a very long period of time (several heart beats). Averaging at least one cardiac cycle results in a nearly constant value for flow. Physically, this value represents the amount of blood flowing, but not the velocity, since it is the integral of all detected velocities.

First, imaging capillary flow yet remains difficult, even in power Doppler mode, partially because blood cells do not scatter much of the transmitted acoustic signal. Small blood vessels, such as the capillaries, provide small fractional blood volume, which further decreases the total backscattered signal. Second, at $1\,\mathrm{mm}\cdot\mathrm{s}^{-1}$, flow velocities in capillary beds are difficult to differentiate from static soft tissue background at zero frequency shift, without being suppressed by the wall filter. This filter is used to prevent tissue motion from being incorrectly ascribed as real flow. In Fig. 17 flow that causes $<$71 Hz frequency shift per Doppler firing is filtered out of the Doppler data to eliminate flow speeds of $<x\,\mathrm{cm}\cdot\mathrm{s}^{-1}$.

The ultrasound machine transmits Doppler pulses every 0.42 ms (recipocal of 2.4 kHz). Backscatter will contain phase shifts between $-\pi$ and $+\pi$, which corresponds to $+23$ and $-23\,\mathrm{cm}\cdot\mathrm{s}^{-1}$ flow speed.

The acoustic wavelength of the color Doppler (CF panel on the right side in Fig. 17) transmits equals 0.385 mm in tissue ($c = 1540\ \mathrm{m}\cdot\mathrm{s}^{-1}$, $Frq = 4\,\mathrm{MHz}$, $\lambda = c/Frq$) and each firing is separated 0.42 ms (recipocal of PRF = 2.4 kHz). The Doppler electronics measures phase shift, therefore it can not measure more than a shift of 2π or $\pm\pi$. Two-pi corresponds to λ or $\pm\pi$ to $\pm\lambda/2$, hence the maximum detectable speed of $v = s/t = 45.8\,\mathrm{cm}\cdot\mathrm{s}^{-1}$, with $s = \lambda/2$ and $t = 1/\mathrm{PRF}$. However this value does not match the displayed $23\,\mathrm{cm}\cdot\mathrm{s}^{-1}$. Doppler pulses work in pulse-echo mode, in which any displacement dx results in a time shift of 2-times dx/c. Finally the maximum detectable flow speed is given by equation 22. For a given wallfilter (WF) the minimal detectable flow is given by the ratio of the PRF to wall filter times the maximum flow, that is, $(2.4\,\mathrm{kHz}/71\,\mathrm{Hz})^{*}23\,\mathrm{cm}\cdot\mathrm{s}^{-1} = 0.68\,\mathrm{cm}\cdot\mathrm{s}^{-1}$.

$$v = \frac{\delta s}{\delta t} = \frac{0.5\cdot c/(2f)}{1/\mathrm{PRF}} = \frac{0.5\cdot 1540/(2\times 3.75\times 10^6)}{1/2.4\times 10^3}$$
$$= 23\,\mathrm{cms}^{-1} \tag{22}$$

3D Imaging

Current ultrasound images are naturally 2D because ultrasound imaging arrays are only 1D. One-dimensional arrays are still predominant in the market. Even so, great efforts in the ultrasound community are pushing ultrasonic imaging toward 2D arrays. The transition from 1D to 2D is especially apparent in the naming scheme of current arrays:

- 1D: Is the classic linear or focused array, which has one row of elements that allows focusing and steering in the lateral imaging plane. The elevational focus is constant due to a fixed elevational curvature of each element.
- 1.25D: Extra rows of elements on either side of the main row allow changes in the elevational aperture, but there is no electronic elevational focusing, nor steering.
- 1.5D: This class of arrays has a 2D set of elements, where the elevational elements are connected symmetrically to the center row. This array can focus in the elevational direction but not steer.
- 1.75D: A 2D set of individually driven elements is available for this type of array, but the number of elements in the elevational direction is much less than in the lateral direction. Elevational focusing is possible, but only limited elevational steering is available.
- 2D: Elevational and lateral directions should be equivalent and indistinguishable for a true 2D array. Full apodization, steering, and focusing is possible in 3D. Currently there are some commercial systems that use 2D arrays particularly in cardiac imaging.

Hardware and software implementations allow the 3D reconstruction of a scanned volume even when using 1D arrays. Sophisticated 3D hardware position sensors allow ultrasound scanners to register the position and orientation of a 1D array in 3D space. Therefore, any acquired image in a set of many can be aligned with others in the set to render a 3D volume (see Fig. 18). However, these hardware additions are costly and can be inconvenient. Moreover, they might show limitations due to interference with electromagnetic fields or nearby metallic objects. Software solutions use correlations between adjacent image frames to determine the transducer translation or rotation. Figure 18 rudimentarily illustrates how individual frames taken in freehand fashion are "stitched" together to form a 3D volume, which can be rendered in various ways. Figure 19 shows an anatomical example of the bifurcation of the ascending carotid aorta rendered as a 3D volume. Some implementations on clinical scanners, however, already use the 4D nomenclature by adding time as the fourth dimension.

CONTRAST IMAGING

As in every other clinical imaging modality, agent based imaging enhancements are available for ultrasonic

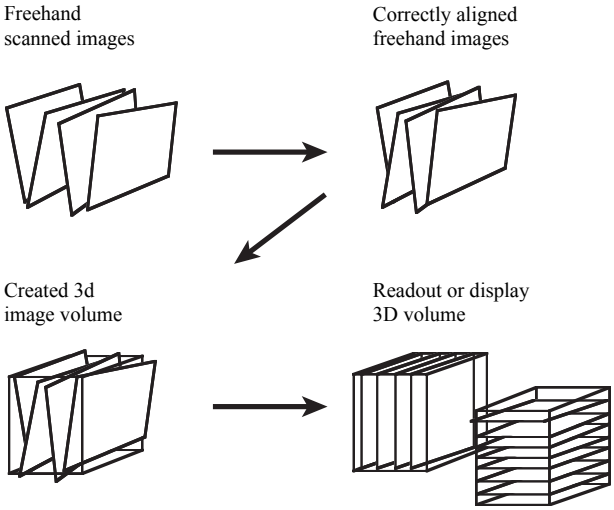

Figure 18. Illustration of 3D image reconstruction. Sets of spatial misaligned images are stacked according to their spatial position and orientation and used to fill a 3D image volume. Afterward this volume can be read out in any slice plane direction or even rendered as a 3D volume, such as shown in Fig. 19.

imaging. However, a limited number of clinical applications is approved by the Food and Drug Administration (FDA). As of 2004, the only FDA approved application for ultrasound contrast agents is for cardiac procedures, and more precisely, for outlining the border of the heart chamber. Other countries or regions such as Europe and Japan have a variety of agents approved. However, considerable research has been performed on ultrasound contrast agents, and it is likely that more FDA approvals will follow in the future. Contrast agents are used to enhance ultrasound image quality; therefore, imaging techniques implemented in current ultrasound scanners will be described.

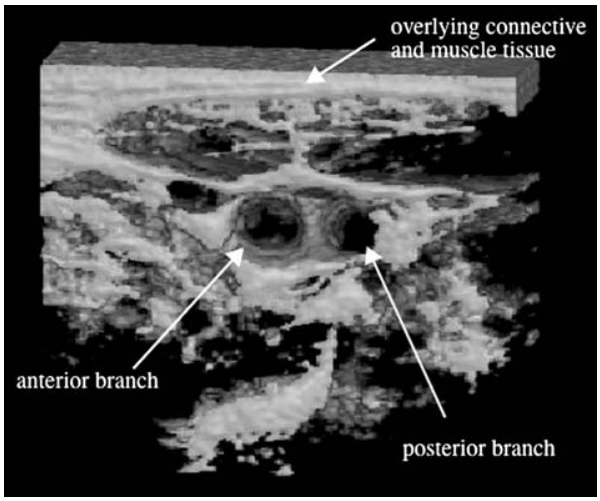

Figure 19. Three-dimensional reconstruction of the ascending carotid artery. This imaging mode uses 3D correlations and compounding to align individual images as the imaging array is swept across the vessel.

Moreover, the physics of contrast agents as well as their optimal clinical use will be discussed.

Clinical Background. Every year 135 million (Source: Amersham Health Inc. owned by GE Healthcare.) ultrasound scans are preformed in American hospitals. Only 0.5% of these procedures actually use contrast-enhancing products. For example, better diagnosis of myocardial perfusion and better visualization of fine capillary-level vasculature will be possible when ultrasound contrast agents are certified by the FDA. Ultrasound is a relatively inexpensive imaging technique, and better diagnostic information can obtained.

New contrast-agent-based ultrasound imaging modes include: Harmonic imaging, Pulse inversion (with harmonic or power mode), Microvascular imaging, Flash contrast imaging, as well as Agent detection imaging.

Enhancing Contrast. A major duty of ultrasound contrast agents is the improvement of ultrasound based image acquisition. The definition of contrast is given in Eq. 23, where I_1 and I_2 are the echo intensities before and after contrast administration, respectively. Even though this is a very simple formula, the mechanism for contrast improvement can be rather complicated.

$$\Lambda = \frac{I_2 - I_1}{I_1} \tag{23}$$

The key for contrast improvement for ultrasonic contrast agents lies in the physical principles of sound transmission, reception, and the nonlinear characteristics of bubbles themselves. For example, an increase in backscatter *amplitude* in the presence of contrast agents relative to the average human tissue backscatter level would improve the overall image. Furthermore, the creation of acoustic *frequencies* that occur in the backscatter signal of bubbles but not in the transmit signal nor in the backscatter of tissue, would provide a mechanism by which bubbles can improve the overall image. An important fact to keep in mind is that ultrasound contrast agents do not enhance the visibility of human tissue nor of blood, but the bubbles themselves can be visualized better than tissue or blood. Nevertheless, imaging perfusion of tissue or measurement of the amount of blood flowing through a vessel can be greatly improved by the usage of ultrasound contrast agents.

Modern Agents. Modern agents are not just gas bubbles. A sophisticated shell coating is used to prevent coalescence and reduce diffusion of the interior gas into the surrounding medium. This shell can be made of serum albumin. Lipids are also used as stabilizing agents. The gases filling the interior of the shell are chosen for low diffusion rates from the bubble into the blood stream as well as because of their low solubility in blood. Table 3 lists commercially available contrast agents. Currently FDA approved contrast agents include Imavist by Alliance Pharma/ Photogen, Definity by Bristol-Myers Squibb Medical Imaging Inc., Albunex by Molecular Biosystems, and Optison by GE/Amersham.

Table 3. Modern Ultrasound Contrast Agents[a]

Manufacturer	Agent Name	Interior Gas	Shell Material
Acusphere	Al-700	Perfluorocarbon	Copolymers
Alliance Pharma. / Photogen	Imavist	Perfluorohexane, air	Surfactant
Bracco	SonoVue	Sulfur hexafluoride	Phospholipid
Bristol-Myers Squibb Medical Imaging, Inc.	Definity	Perfluoropropane	Lipid bilayer
	MRX-815-stroke	Perfluoropropane	Lipid bilayer
Molecular Biosys.	Albunex	Air	Albumin
	Oralex	Air	Dextrose
GE/ Amersham	Optison	Perflutren	Albumin
Nycomed Imaging AS	Sonazoid	Perfluorobutane	Lipid
Schering AG	Echovist	Air	Galactose
	Levovist	Air	Lipid layer
Sonus Pharma.	EchoGen	Dodecafluoropentane	Albumin
	SonoGen		Charged surfactant

[a]See Refs. 3,7, and 9.

Acoustic Bubble Response. Ultrasound contrast agents can be viewed as systems known as harmonic oscillators, with a given amplitude, phase, and frequency. Min-naert has derived Eq. 24, which gives the resonance frequency of a gas bubble as a function of its size. For example, a 3 μm radius (R_0) air bubble (adiabatic coefficient κ) in water (mass density ρ_L) under atmospheric pressure P_0 has a resonance frequency f of 1.1 MHz (Table 3). This is a very fortunate relationship since capillaries of the human circulatory system are as small as 8 μm in diameter and typical clinical frequencies used are 1–10 MHz.

$$f(R_0) = \frac{1}{2\pi}\frac{1}{R_0}\sqrt{\frac{3\kappa P_0}{\rho_L}} \tag{24}$$

The amount of acoustic scattering of the bubble surface (scattering cross-section σ_S) is described by the Rayleigh equation. This equation is used for scatterers that are small (μm) relative to the acoustical wavelength used (mm). For gas bubbles in water, the Rayleigh equation can be written with a series of mathematical terms for corresponding physical oscillation modes.

$$\sigma_S = 4\pi a^2 (ka)^4 \left[\left(\frac{\kappa - \kappa_0}{3\kappa} \right)^2 + \frac{1}{3}\left(\frac{\rho - \rho_0}{2\rho + \rho_0} \right)^2 \right] \tag{25}$$

The first term represents a monopole type bubble oscillation, whereas the second term describes a dipole term. One can see that the monopole term dominates the scattering due to the large compressibility (κ) difference between water and air–gas. Density differences (ρ) between water and air/gas are large too, however, the monopole term dominates the acoustic scattering (see Table 4).

Mathematical and Physical Modeling. The equation of motion of a bubble can be readily derived from an energy balance of kinetic (T) and potential energies (U) using the Lagrange formalism ($L = T - U$). It should be mentioned that the momentary inertial mass of the bubble as an oscillator does change with time. This is a major reason why ultrasound contrast agents are nonlinear systems, as will be shown shortly. One of the first equations describing the motion of a gas bubble excited by ultrasound was derived by Rayleigh–Plesset and is given in Eq. 26. This formula is derived under the assumption that the interior gas follows the ideal gas law, and other forces acting on the bubbles are comprised of the internal vapor pressure p_d, the external Laplace pressure caused by the surface tension σ, the viscosity η_L of the surrounding host medium (water), the mass density ρ_L of the water, as well as the static p_0 and acoustic $p_\infty(t)$ pressures.

$$R(t) = \frac{1}{R(t)}\left(-\frac{3}{2}\left(\frac{\partial}{\partial t} R(t) \right)^2 + \frac{1}{\rho_L}\left(\left(p_0 + \frac{2\sigma}{R_0} - p_d \right)\left(\frac{R_0}{R(t)} \right)^{3\kappa} + \cdots + p_d - \frac{2\sigma}{R(t)} - \frac{4\eta_L \frac{\partial}{\partial t} R(t)}{R(t)} - p_0 - p_\infty(t) \right) \right) \tag{26}$$

Figure 20 shows a simulation of the bubble response to a short tone burst excitation. Transmitted acoustic pressures of 1 and 50 kPa were simulated. Graph (a) shows a 1.1 MHz and 50 kPa pressure waveform as transmitted by a simulated ultrasound transducer. Graph (c) shows the subsequent radial oscillations of the simulated bubble (resting radius of 3 μm). Graph (b) shows the spectral response of these oscillations for a sound pressure of 1 kPa. The bubble oscillates mostly at the driving frequency of 1.1 MHz. An increase in sound pressure amplitude (i.e., 50 kPa) reveals the nonlinear nature of gas bubbles. In panel (d), in addition to 1.1 MHz one can also see higher harmonics of 2.2 MHz, 3.3 MHz, and so on.

Table 4. Scattering Coefficients for Monopole and Dipole Terms in Eq. 25 of a Water or Air Filled Sphere Under Water

Material	Bulk Modulus κ, MPa	Density ρ, $kg \cdot m^{-3}$	Monopole Magnitude	Dipole Magnitude
Water	2250	1000	0	0
Air	0.14	1.14	2.9×10^7	0.33

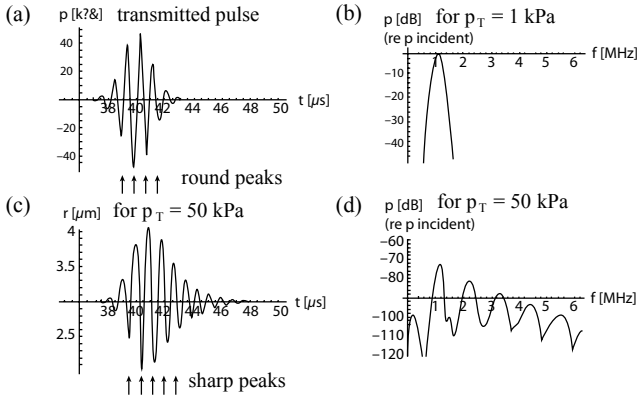

Figure 20. For higher transmit sound pressures (p_T) gas bubbles exhibit nonlinearities at similar magnitudes as the fundamental frequency [(b) vs. (d)]. Higher harmonics increase in their relative amplitude with sound pressure. Radials oscillations of the gas bubble contrast agent shows the nonlinear response during the compressional phase (arrows at small radii). Harmonic imaging takes advantage of the strong nonlinear character of contrast agent, which can be stronger than tissue depending on the number density of the bubbles.

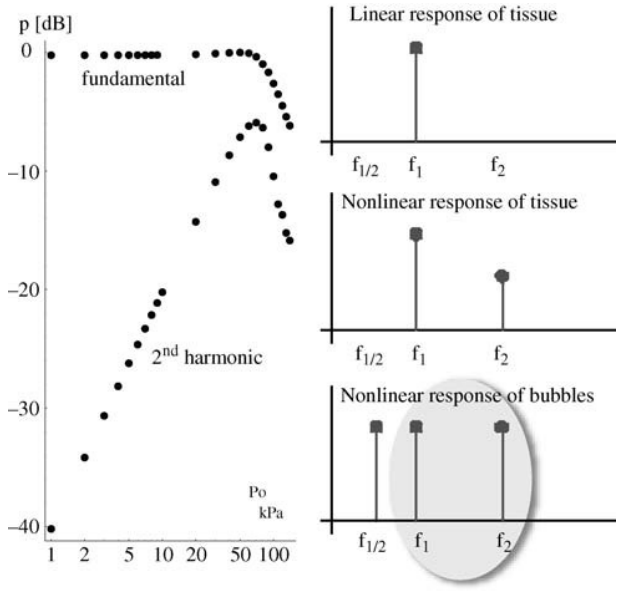

Figure 21. Higher harmonics increase in their relative amplitude with sound pressure (left), P_{harmonic}/P_0. Harmonic imaging takes advantage of the strong nonlinear character of contrast agent, stronger than tissue, depending on the number density of the bubbles. Subharmonic emissions $f_{1/2}$ are also characteristic for bubbles.

Modern ultrasound contrast agents cannot be modeled using the free gas bubble Rayleigh–Plesset model. Elastic layer-based models presented by de Jong (5), Church (4), and Hoff (10) contain additional parameters, such as the mass density of shell material, a second surface tension term, a second viscosity term, or the elastic modulus of the shell material.

Imaging Modes

The following sections will cover imaging modes that rely on nonlinear backscatter, either originating from body tissue or due to nonlinear reflections from contrast agents. Each mode will be theoretically described and illustrated with examples.

Harmonic Imaging

Nonlinear tissue and contrast agent backscatter is the basis for harmonic imaging. Human tissue, as well as ultrasound contrast agent, can be driven in a nonlinear fashion such that the backscattered signal contains not only the original frequency f_0, but also $2x\,f_0$, $3x\,f_0$, and so on (see Fig. 20d). Higher harmonics increase in their relative amplitude with sound pressure. Harmonic contrast imaging takes advantage of the strong nonlinear character of contrast agent, which is stronger than tissue. As a result, nonlinear backscatter from tissue will be smaller in amplitude than that of contrast agent and the vascular system will be visible over tissue. Subharmonic emissions are also characteristic for bubbles ($1/2x\,f_0$, $1/3x\,f_0$, etc.) and can be used to distinguish bubbles from tissue.

Figure 21 is comprised of a direct gas bubble simulation and an illustration of harmonic bubble behavior. As can be seen from the simulation results, harmonic scattering of gas bubbles increases with increasing incident sound pressure. Specifically, the normalized amplitudes of the fundamental and the second harmonic frequency are shown here ($p_{\text{fundamental}}/p_0$ and p_{harmonic}/p_0). Increasing the incident sound pressure causes a proportional increase in the fundamental response, while the contribution of the harmonics increases more strongly. At 50–100 kPa, the backscatter amplitude of the second harmonics peaks and for higher pressures more and more energy is distributed over a wide range of frequencies, from sub-harmonics f_0/n to higher harmonics n^*f_0. Because the model as described in Eq. 26 does not take into account any losses, such as those induced by radiation or viscous damping, backscatter predictions for large excitation pressures will not be accurate. However, at modest amplitudes tissue scatters in a linear fashion, gas bubbles contribute harmonic signals, and the amplitude ration between fundamental and harmonic components can approach 1 for bubbles driven at sufficiently large amplitudes (illustration in lower right panel of Fig. 21).

Figure 20 shows the oscillation of a gas bubble in a large amplitude acoustic field. Panel (a) shows the excitation sound pressure waveform of 50 kPa amplitude. Radial excursions as well as the sound pressure spectrum at a distance of 5 cm from the bubble are plotted on the bottom panels (c) and (d), respectively. Most notably are the sharp peaks for bubble radii smaller than the initial bubble radius (see arrows in Fig. 20c). At positive incident sound pressures, the bubble is compressed and exhibits a large internal pressure. At the same time, the bubble's resonance frequency changes. This change in resonance is the reason

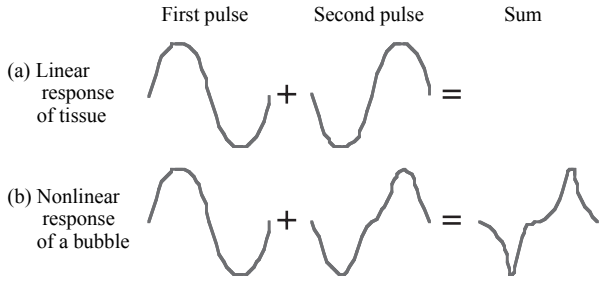

Figure 22. Tissue and contrast agent can yield different backscatter when exposed to an acoustic field of moderate intensity (typically of an mechanical index (MI) of less then 0.2). (a) Tissue responds in a linear fashion, that is, it yields a 0 and a 180° phase-shifted signal. The sum of both waves is zero. (b) For ultrasound contrast agent, the backscatter will include higher harmonics. A 180° phase shift in the transmit frequency f_0 will result in a 360° phase shift in the second harmonic $2f_0$. However, a 360° phase shift will result in the original signal. Therefore, the sum of a regular pulse and a inverted pulse will cancel for f_0 frequency components but not for $2f_0$ components.

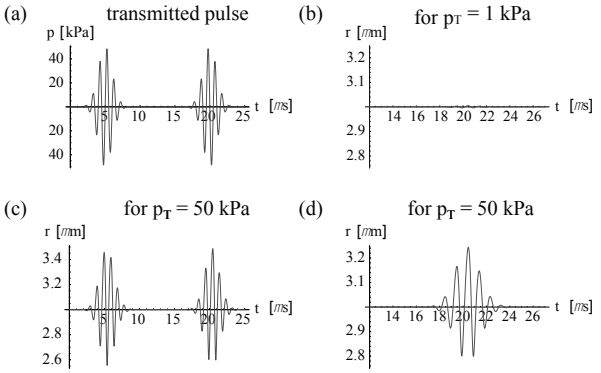

Figure 23. Two transmitted pressure waveform pulses with 180° phase shift with respect to each other, are displayed at time equal 5 and 20 μs in panel (a). This concept of inverted pulses is illustrated in Fig. 22(a). For 1 kPa sound pressure amplitude the sum of the oscillations of these two pulses is near zero (b). However, for a sound pressure of 50 kPa, the radial excursions of the contrast agent bubbles is nonlinear (as shown in Fig. 20) and the sum of the 0 and 180° signal is almost as great (3.2 μm in d) as the oscillation itself (3.4 μm in c). This technique is used in pulse inversion contrast agent detection scheme.

for their highly nonlinear character. Panel (b) shows the scattered sound pressure spectrum for a low incident pressure of 1 kPa. No harmonic contributions can be seen within 40 dB of the pressure amplitude at the fundamental frequency.

Pulse Inversion Mode

As its name suggests, pulse inversion uses inverted pulses to gain contrast in the image. Figure 22 illustrates how this imaging mode works. As opposed to regular B-mode imaging, this mode requires *two* transmissions per image line. The first transmission does not differ from regular B-mode. However, the second transmission is 180° phase shifted, that is, inverted with respect to the first pulse transmitted. In case of tissue the backscatter for both pulses will mostly remain the same in magnitude. However, contrast agents respond with harmonic contributions which differ for 0 and 180° pulses. For very low acoustic pressures, this difference might not be distinguishable from the linear backscatter, but a mechanical index of 0.2 or less is sufficient to perform pulse inversion imaging. The mechanical index is a measure for the sound pressure amplitude and will be defined in the bioeffects section.

High sound pressure amplitude pulses can have two effects. First, they cause nonlinear tissue backscatter, thus reducing the contrast between tissue and contrast agent in the vascularity. Second, they destroy the contrast agent. One has to keep in mind that contrast agents are comprised of encapsulated gas bubbles. Therefore the bubble can shatter and the contained gas can subsequently dissolve into the blood pool. This shattering is possibly a source for bioeffects of ultrasonic imaging and will be discussed in a later section.

Theoretical modelling of the oscillatory behavior of gas bubbles using the above-introduced model directly shows the nonlinear response of gas bubbles. Figure 23a shows the two-pulse sequence required for pulse inversion imaging. For transmit pressures of 1 kPa, the difference in bubble response to 0 and 180° is very small. However, on the same scale, the response to a 50 kPa excitation yields two signals whose fundamentals f_0 cancel, but whose second harmonic contributions $2f_0$ add in phase (see Figs. 22 and 23 d).

A major downside of pulse inversion imaging is its sensitivity to motion. Spatial shifts cannot be distinguished from changes in back-scatter due to changes in transmit phase. A clever work-around to this problem is illustrated in Fig. 24, where a three-pulse transmit of varying phase is shown. Situations in which motion is anticipated or intestinal peristalsis or chest wall excursions during breathing. The latter is on the order of $2\,\mathrm{cm}\cdot\mathrm{s}^{-1}$, or for a 1 kHz PRF, 20 μm per firing. A signal of 1 MHz center frequency will experience a phase shift of 4.8° when spatially translated 20 μm. It is assumed that the time duration in which the three pulses are fired is small compared to that of the body motion. If so, then the motion can be approximated as being linear on the time scale of the firings. The first firing is transmitted with zero phase, the second one with $5 + 180°$, the third one with 10° phase shift. Linear response of tissue will result in backscatter signals of 0°, 5°+180°, and 10° phase shifted signals. Averaging the first and third backscatter signal will yield an average of 5° phase shift. Adding this average signal to the second backscatter signal will yield a value of zero for linear tissue, even while it is in motion. Bubbles, however, will yield a similar, nonzero, signal whether in motion or not.

Coded Excitation and Coded Harmonic Excitation. *Coded excitation* is a way to overcome poor signal to noise ratios (SNR) in ultrasonic imaging. It was already used in radar imaging for the same purpose, before its introduction to medical ultrasound. The most simple solution for poor

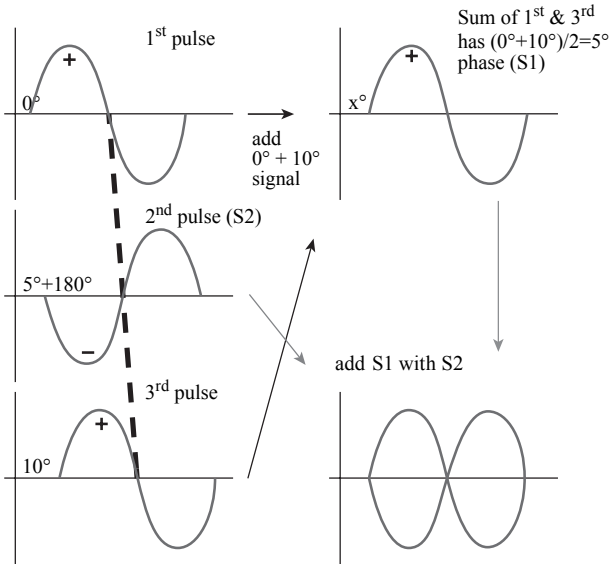

Figure 24. A three pulse sequence with a linear shift in transmit phase (0°, 5°+180°, and 10°) is used to suppress tissue signal, even when the tissue is in motion. The 0 and 10° backscatter signals are averaged to yield a 5° signal from tissue (SI). The 5° phase-shifted and inverted transmit signal (S2) is then added to the averaged signal SI. For moving tissue the result will be zero. If the tissue motion is linear during the time span of the three transmit pulses (~1 ms), then pulse will be separated by an offset of x°. This offset is in addition to the initial 5° offset between first & second and second and third pulse. Therefore tissue will yield zero for S1+S2. Ultrasound contrast agents, however will yield S1≠S2 as shown in Figs. 22 and 23.

signal/noise ratios is to increase the amplitude of transmitted sound. However, the FDA regulates sound pressure amplitudes because of the likelihood of acoustic cavitation in the presence of large sound pressure amplitudes. Moreover, the number of acoustic transmissions per unit time (pulse repetition interval, PRI) as well as the length of individual pulses (burst length) are regulated by means of the overall deposited energy that will eventually result in tissue heating. Both effects will be discussed in the Bioeffects section below. In addition to regulatory and safety concerns, increasing the number of cycles in a traditional transmit pulse also reduces the axial resolution.

However, improvements in signal to noise ratios without sacrificing axial resolution can be achieved despite regulations on pressure amplitudes and burst lengths. Transmission of specially designed and unique signals can significantly improve their detectability. This concept is called Coded harmonic excitation.

Various code types shall be discussed here to illustrate how Coded excitation works. Figure 25 illustrates two codes. On the left side is the most simple code, a so-called pulse train (or uncoded tone burst), that is, a series of pulses or sinusoids. When transmitting four cycles at a certain frequency one can use a frequency filter that is sensitive at the transmit frequency, but only for signals that are four cycles long. A more complicated type of coded excitation is the code shown on the right side of Fig. 25.

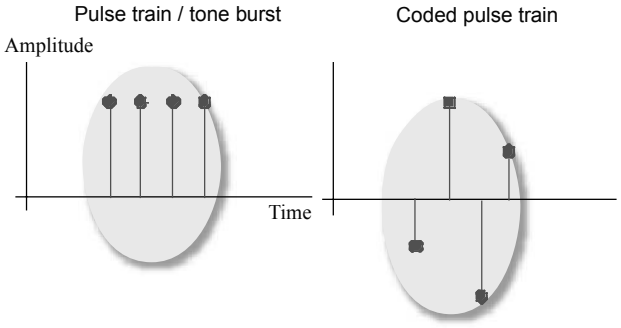

Figure 25. Some signal to noise problems can be overcome by the use of coded excitation. Instead of a single pulse, a pulse train (commonly also known as a tone burst) or coded pulse train is transmitted for better backscatter detection. See Fig. 26 for temporal /spatial resolution.

This signal also transmits four cycles, but now the four cycles all differ in sign as well as in amplitude. Both features make this code more unique and therefore more detectable when ambient noise lowers SNR.

Above mentioned frequency filters are explained in Figs. 26 and 27. The first column in Fig. 26 illustrates the transmit pressure waveforms and the second column shows the receive filter used. A mathematical technique termed convolution is used to match the transmitted waveform with the anticipated receive signal by means of an appropriately designed filter. The average reader might not have adequate signal processing background to be familiar with this concept. Therefore, Fig. 27 will be used to explain Coded Excitation for the example of Golay code

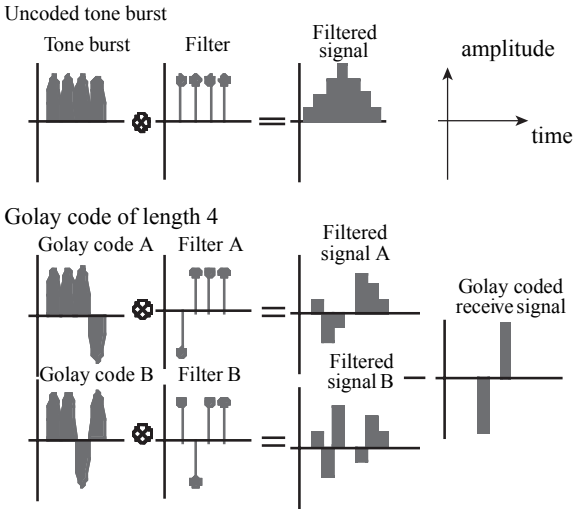

Figure 26. Coded excitation is implemented on modern ultrasound scanners to overcome signal loss and low SNR. A simple solution is the increase in burst length. However, this simultaneously results in a decrease in axial/temporal resolution. Specially coded waveforms are designed for an increase in SNR by reasonably maintaining spatial resolution. Golay codes, for example, can be designed for a 10-fold increase in SNR by loosing only a factor of two in temporal resolution.

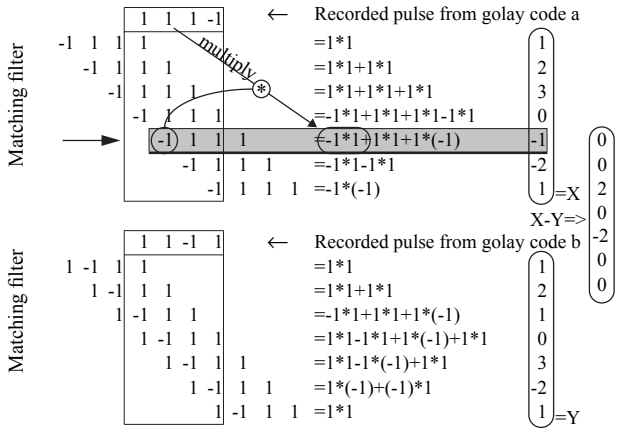

Figure 27. The mathematical process of convolution is described in this figure. For this purpose the reader should refer to the Golay code of length 4 given in Fig. 26 and to the text section on Coded excitation for a detailed description.

of length 4 (see Fig. 26). This code consists of two transmit pulse packages. The first and second packages are four pulse sequences of [+1, +1, +1, −1] and [+1, +1, −1, +1], respectively. Such pulses are shown on the top row of each box in Fig. 27. The pulses are transmitted into the body and the resulting echoes, which should show the same pattern, are recorded. Matching filters are shown below the pulse packages and have been replicated at a total number of 7 positions. Each filter replication has an overlap with the transmit pulse ranging from 1 to 4 digits. For a given position, numbers in the same column are multiplied and then the resulting values of the overlapping columns are added.

For clarification the highlighted case in the top system for position 5 (arrow) is explained in detail. The filter [−1, 1, 1, 1] and the recorded pulse [1, 1, 1, −1] overlap for three digits and the computational method of convolution is equivalent to computing the inner product of two vectors: $[1, 1, -1]^*[-1, 1, 1] = 1^*(-1)+1^*1+(-1)^*1$, which sum to −1. This value is displayed in the column on the right. This convolution procedure is done for both transmits. Subtracting the two resulting 7 digit vectors $X = [1, 2, 3, 0, -1, -2, 1]$ and $Y = [1, 2, 1, 0, 3, -2, 1]$ will yield [0, 0, 2, 0, −2, 0, 0], a receive vector (called Golay-coded receive signal in Fig. 26) with good temporal/spatial resolution. In the given case it is essentially three time steps long: [−2, 0, 2]. The uncoded tone burst is 7 time steps long (see top of Fig. 26).

Back to Fig. 26, the result of the convolution is shown in the third column. For the uncoded tone burst one can see a triangular shaped signal that peaks where the receive filter perfectly matches the incoming pressure wave. The temporal duration of the convolution increases as the duration of the tone burst increases. This unwanted effect of loss of spatial resolution is overcome by the use of more sophisticated codes. Golay transmit codes and receive filters, for example, can mostly maintain spatial resolution while improving SNR. Two differing transmit codes are used and the resulting convolutions are subtracted from each other, similar to pulse inversion imaging.

Coded excitation in the form of a Chirp-type pulse train yields a signal to noise gain of $\sqrt{\Delta F\, T}$; for example, a signal with a 1 MHz frequency sweep and $T = 16\,\mu$s pulse duration will yield a fourfold increase in SNR, which corresponds to 12 dB. Chirps are tone burst of continuously increasing transmit frequencies within the pulse train. Continuously in frequency decreasing pulse trains are called pirchs, which almost spells chirp backward. General Barker and Golay codes perform well too. For a standard Barker sequence the side lobe amplitudes of the transmit/receive signal are −22 dB down relative to the amplitude main lobe. A Golay code with 16 pulses per burst yields a ten-fold increase in SNR. Here, only a length-4 sequence is shown for clarity (see Fig. 26).

More detailed mathematical background, as well as clinical feasibility can be found in publications by Nowicki (19) and Misaridis (20), for example.

BIOEFFECTS

Ultrasound related bioeffects are centered on two main categories: cavitation and heating. Acoustic output (and therefore to some degree acoustic cavitation) is regulated by the FDA through the implementation of the mechanical index (MI), as well as the temperature index (TI) in the so-called Output Display Standard (Standard for Real Time Display of Thermal and Mechanical Acoustic Output Indices on Diagnostic Ultrasound Equipment (1992), published by the National Electrical Manufacturers Association as UD-3). The output display standard is used to obtain approval by the FDA for medical use of ultrasound scanners.

Cavitation is a well-studied effect and manifests itself, for example, by the erosion of ship propellers and for therapeutic purposes in lithotripsy. Hydrodynamically generated microscopic gas bubbles imploding in close proximity to the metallic surface of the propellers punch small holes into the metal. This occurs due to the existence of water jets generated by asymmetrically imploding gas bubbles.

To date, there are only very limited clinical reports on the occurrence of bioeffects in diagnostic ultrasound. Nevertheless, *in vitro* cell cultures and animal models are used to study bioeffects at acoustic parameters beyond the limits for diagnostic imaging. No limits for single parameters (e.g., pressure amplitude, wave frequency, or pulse length) were identified *per se due* to the complicated biological end points (21). However, two fundamental quantities, MI and TI, were introduced as parameters by which to judge the probability of bioeffects (11,21). Both quantities gain in presence, especially with the MI being used by the FDA to limit the acoustic output of scanners.

$$\mathrm{MI} = \frac{p[\mathrm{MPa}]}{\sqrt{f[\mathrm{MHz}]}} \quad \mathrm{TI} = \frac{W\, p\,[\mathrm{Nm \cdot s^{-1}}]}{W_1^o\,[\mathrm{Nm \cdot s^{-1}}]} \tag{27}$$

Pressure p and frequency f are quantities that can be directly measured experimentally. Power W_p, however, is a derived quantity and is related to the pressure waveform as

shown in Eq. 28 (22).

$$PII = \frac{\int_{t_1}^{t_2} v_h(V(t))^2 dt}{10^4 \rho c M_L(f_c)^2} \left[\mathrm{J \cdot cm^{-2}}\right] \tag{28}$$
$$I_{\mathrm{SPTA}} = \mathrm{PII}(j, v, z_{mj\mathrm{PII}}) \times \mathrm{PRF}\,[\mathrm{W \cdot cm^{-2}}]$$

The pulse intensity integral *PII* is computed over a truncated duration of the acoustic wave, namely, from t_1 to t_2. These times correspond to the 10 and 90% indexes of the accumulated total energy in the tone burst and can in most circumstances be regarded as the burst length. When calibrating an acoustic transmitter, one often measures an electric waveform produced by a underwater microphone, called a hydrophone. A conversion function v_h, is then used to determine the actual pressure of the measured electric waveform $V(t)$. M_L is the hydrophone's frequency dependence. Together, v_h, and M_L allow the complete conversion of the electrical hydrophone signal to the pressure of the measured wave. Mass density and speed of sound of the medium in which the wave travels are labeled as ρ and c. Even when the burst length is taken into account, one does not know the total transmitted power without the PRF. Spatial peak and temporal average intensities (I_{SPTA}) are computed with knowledge of the PRF, yielding units of watts per centimeter squared ($W \cdot \mathrm{cm}^{-2}$). For computing the TI, however, one needs to multiply that value with the geometric cross-section of the acoustic beam. In reality, the computation of the TI is more complicated and takes into account more parameters such as the chosen exposure conditions, as well as nominal perfusion parameters. In clinical use, perfusion parameters are estimated from user selected target tissue types.

An additional step toward reducing the possibility of bioeffects is the usage of the principle of ALARA (as low as reasonably achievable), that is, the reduction of acoustic output and reduction of exposure time to the lowest reasonable minimum. Typical diagnostic acoustic procedures operate at or below the FDA limit for $I_{\mathrm{SPTA.3}}$ of $720\,\mathrm{mW \cdot cm^{-2}}$ (see Table 5 and (23)). Currently, the FDA regulates output limits via Tracks 1 and 3 of 510(k). Track 1 uses the I_{SPTA} levels shown in Table 5, whereas Track 3 allows device manufacturers to increase their output to a general $720\,\mathrm{mW \cdot cm^{-2}}$ if their device provides user feedback via MI and TI display standards (24).

Biological effects of ultrasound can be investigated after the acoustic output of a sound source is quantified and qualified as described in the previous paragraphs. *In vitro* cell studies are typically the first method for research on the biological effects of ultrasound. Such studies can be performed in a highly controlled environment and are therefore repeatable. This is not necessarily the case for patient studies where many factors cause unavoidable variabilities.

It was found in a study on anesthetized rats that the interaction of the incident sound field with ultrasound contrast agent can cause pete-chial hemorrhages (punctuate sites of bleeding from blood vessels) in heart tissue. In a study by Li et al. (13,14) ultrasound contrast agents were injected in a similar fashion as is used in clinical contrast echocardiography. Heart tissue was observed in real time using a phased array ultrasound scan head (1.7 MHz transmit frequency) operating in a harmonic mode native to the clinical scanner used. Postmortem heart tissue analysis showed that bleedings scaled monotonically, proportionally to the square of the peak rarefactional pressure ($\mathrm{P_{rare}}$) amplitude of the sound field. Pressure amplitudes of 0.6–1.8 MPa P_{rare} were used in that study. This pressure range corresponds to MIs between 0.5 and 1.5. Real-time ultrasonic imaging showed that premature ventricular contractions (PVC) were triggered by ultrasound in the presence of contrast agents. However, no significant PVC were observed for MIs of 0.5 and 1.0, but up to 40 PVCs were observed for a 3 min exposure at a MI of 1.9, the maximum allowed by the FDA.

Currently, there are very limited clinical reports on unanticipated bioeffects of ultrasound. Intended effects exist since ultrasound can be used to treat kidney stones and during such procedures it is likely that tissue bleeding occurs. There have been reports of effects associated with diagnostics, but the review of these reports has yielded no establishment of a causal relationship with ultrasound exposure. However, a study by van der Wouw in healthy male volunteers concludes:"Imaging of contrast agents with high acoustic pressures can cause PVCs if end-systolic triggering is used. This effect is related to both the dose of contrast agent and acoustic pressure. It does not occur during end-diastolic triggered imaging. Precautionary measures would include using lower MIs or end-diastolic triggering" (25).

It has been seen that the level of bioeffects varied with the ultrasound contrast agent used. This is probably due to different shell materials and internal gases, which cause the bubbles to oscillate at different amplitudes. If agent rupture occurs, cavitation type damage in produced in the surrounding tissue (13,14). Thermal and nonthermal effects exist and they are under investigation. According to Natori (26) temperature increases of no more than 1.5°C above normal are considered clinically acceptable and nonthermal, that is, cavitation based effects can only be found where gas bodies are present, such as postnatal lung and intestines, or via ultrasound contrast agents. Therefore regular B-mode imaging is considered by many unaffected (26).

Finally, it should be mentioned that there are no bioeffects in the absence of contrast agent and also no bioeffects in the presence of contrast agents but absence of an ultrasonic field. Moreover, low doses ($10–50\,\mu\mathrm{L \cdot kg^{-1}}$)

Table 5. Acoustical Output Limits for Clinical Ultrasound Scanners per FDA Regulation

Tissue	$I_{\mathrm{SPPA.3}}$, $\mathrm{mW \cdot cm^{-2}}$	$I_{\mathrm{SPTA.3}}$, $\mathrm{W \cdot cm^{-2}}$	MI
Peripheral vasculature	720	190	1.9
Cardiac	430	190	1.9
Fetal and other	94	190	1.9
Ophthalmic	17	28	0.23

[a]Intensity values are derated for tissue attenuation with an acoustic attenuation of $0.3\,\mathrm{dB \cdot cm^{-1} \cdot MHz^{-1}}$.
[b]I_{SPTA} and MI are defined in the text, I_{SPPA} is defined as the intensity of the spatial peak pulse averaged waveform.

of ultrasound contrast agent yielded little if any bioeffects. In general, radiological contrast agents, or the imaging procedure itself, may bear the risk of bioeffects. That risk has to be balanced with the medical need for the procedure.

ACKNOWLEDGMENTS

I wish to thank Katy, Kim, Mario, John, and Jessi for their invaluable efforts for proof reading and their technical comments. Also, I would like to thank the reviewers for their contributions and very helpful commentary. Most of all, I wish to thank my wife Naki for her patience during many lost hours of family time.

BIBLIOGRAPHY

1. Angelsen BAJ. Ultrasound Imaging Waves, Signals, and Signal Processing; 2000.
2. Averkiou M, et al. Ultrasound contrast imaging research. Ultrasound Q 2003;19:(1):27–37.
3. Becher H, Burns PN. Handbook of Contrast Echocardiography—LV Function and Mycardial Perfusion. Berlin: Springer-Verlag; 2000.
4. Church CC. The effects of an elastic solid surface layer on the radial pulsations of gas bubbles. J Acoust Soc Am 1995; 97(3):1510–1521.
5. deJong N, et al. Absorption and scatter of encapsulated gas-filled microspheres: Theoretical considerations and some measurements. Ultrasonics 1992;30:95–105.
6. Duck FA. Physical Properties of Tissue. San Diego: Academic Press; 1990.
7. Feinstein SB. The powerful microbubble: From bench to bedside, from intravascular indicator to therapeutic delivery system, and beyond. Am J Physiol Heart Circ Physiol 2004;287: H450–H457.
8. Gray H, Williams PL, Bannister LH. Gray's anatomy: The anatomical basis of medicine and surgery. New York: Churchill Livingstone; 1995.
9. Grayburn PA. Current and future contrast agents. Echocardiography 2002;19(3):259–265.
10. Hoff L. Acoustic characterization of contrast agents for medical ultrasound imaging. Ph.D. dissertation at the Norwegian University of Science and Technology in Trondheim, Norway; 2000.
11. Holland CK, Apfel RE. Thresholds for transient caviation produced by pulsed ultrasound in a controlled nuclei environment. J Acoust Soc Am 1990;88(5):2059–2069.
12. Kasai C, Namekawa K, Koyano A, Omoto R. Real-time two-dimensional blood flow imaging using an autocorrelation technique. IEEE Trans, Ultrasonics, Ferroelectrics, Frequency Control 1985;SU-32(3):458–464.
13. Li P, Cao et al. Impact of myocardial contrast echocardiography on vascular permeability: An in vivo dose response study of delivery mode, pressure amplitude and contrast dose. Ultrasound Med Biol 2003;29(9):1341–1349.
14. Li P, Armstrong WF, Miller DL. Impact of myocardial contrast echocardiography on vascular permeability: Comparison of three different contrast agents. Ultrasound Med Biol 2004; 30(1):83–91.
15. Lindsay RB. The story of acoustics. J Acoust Soc Am 1965; 39(4):629–644.
16. Shung KK, Zipparo M. Ultrasonic transducers and arrays. IEEE Eng Med Biol 1996; 20–30.
17. Angelsen BAJ, et al. Which transducer array is best. Eur J Ultrasound 1995;2:151–164.
18. McDicken WN, Evans DH. Doppler Ultrasound: Physics, Instrumentation and Signal Processing. New York: John Wiley & Sons, Inc.; 2000.
19. Nowicki A, Litniewski J, Secomski W, Lewin PA. Estimation of ultrasonic attenuation in a bone using coded excitation. Ultrasonics 2003;41:615–621.
20. Misaridis TX, et al. Potential of coded excitation in medical ultrasound imaging. Ultrasonics 2000;38:183–189.
21. Abbott JG. Rationale and derivation of Mi and Ti—A review. Ultrasound Med Biol 1999;25(3):431–441.
22. American Institute of Ultrasound in Medicine (AIUM). Standard Specification of Echoscope Sensitivity and Noise Level Including Recommmended Practice for Such Measurements; 1978.
23. O'Brien WD, et al. Acoustic output upper limits proposition. J Ultrasound Med 2002;21:1335–1341.
24. Nyborg WL. History of the American Institute of Ultrasound in Medicine's efforts to keep ultrasound safe. J Ultrasound Med 2003;22:1293–1300.
25. van derWouw PA, et al. Premature ventricular contractions during triggered imaging with ultrasound contrast. J Am Soc Echocardiogr 2000;13(4):288–294.
26. Natori M. Ultrasound safety: Overview and what we do need in daily clinics for a safe use of diagnostic ultrasound. Inter Congress Ser 2004;1274:125–128.

See also COMPUTED TOMOGRAPHY; ECHOCARDIOGRAPHY AND DOPPLER ECHOCARDIOGRAPHY; IMAGING DEVICES; MAGNETIC RESONANCE IMAGING.

ULTRAVIOLET RADIATION IN MEDICINE

J. J. LLOYD
Regional Medical Physics Department
Royal Victoria Infurmary
Newcastle-upon-Tyne,
United Kingdom

INTRODUCTION

It is to the philosophers and physicians of the ancient civilizations that we should attribute the earliest history of ultraviolet radiation (UVR) in medicine (1). For example, the Greek sun god, Apollo, was also the spiritual god of healing, providing the first documentation of an association between sunlight and health. In 525 BC, Herodotus observed that the strength of a human's skull was related to sunlight exposure, >2000 years before the formal discovery of the role of sunlight in vitamin D metabolism. At about the same time the Egyptians were using psoralens from plant extracts and sun exposure in the treatment of vitiligo. However, it was not until Jonathan Ritter in 1801 discovered the UV region in the solar spectrum that the science of photobiology could really begin.

The Danish physician Niels Finsen (1860–1904) is regarded by many as the father of modern UV therapy. In a series of articles published between 1893 and 1896,